SINGLE AND TWO-PHASE CONVECTION IN FLEXIBLE PDMS MICROCHANNELS WITH MICROPILLAR ARRAYS

A Dissertation
Presented to
The Academic Faculty

by

Nikhil Damle

In Partial Fulfillment
of the Requirements for the Degree
Master's in the
School of Mechanical Engineering

Georgia Institute of Technology
May, 2021

SINGLE AND TWO-PHASE CONVECTION IN FLEXIBLE PDMS MICROCHANNELS WITH MICROPILLAR ARRAYS

Approved by:

Dr. Yogendra Joshi, Advisor
School of Mechanical Engineering
Georgia Institute of Technology

Dr. Satish Kumar
School of Mechanical Engineering
Georgia Institute of Technology

Dr. Vanessa Smet
School of Mechanical Engineering
Georgia Institute of Technology

Date Approved: January 5th, 2021

To

Aai, Baba, Dada, Ajji, and Ajoba

(My parents, brother, and grandparents)

ACKNOWLEDGEMENTS

I would like to sincerely thank Prof. Yogendra Joshi for giving me the opportunity to pursue research and study a novel problem at the Microelectronics and Emerging Technologies Thermal Laboratory at Georgia Institute of Technology. His guidance and support throughout my time at Georgia Tech have helped me immensely in developing a practical level understanding of the field of Thermal Engineering.

I would also like to thank Prof. Satish Kumar, a member of my reading committee and a course instructor, for all the valuable feedback and his teachings in numerical heat transfer, and Prof. Vanessa Smet, member of my reading committee, for her support with the GT-PRC cleanroom. Prof. Satish Kumar, Prof. Peter Loutzenhiser, and Prof. Devesh Ranjan were instrumental in helping me develop a theoretical understanding of thermofluids for which, I am grateful.

This work would not have been completed without the help of many friends, students, and staff at Georgia Tech. First, I would like to thank Prof. Wayne Whiteman and Camellia Henry from the School of Mechanical Engineering for their continued and prompt support, and Lila Dahal from GT-PRC cleanroom, for his technical cleanroom assistance. Second, I would like to thank my fellow labmates at METTL for their friendship and support: Dhaval Patel, Shuvajit Dey, Joon Woo Kim, Justin Broughton, Wenming Li, Arash Nayebzadeh, Pouya Asrar, and Daniel Lorenzini. Third, I would like to thank the Graduate Student Government Association and my friends at Georgia Tech for making my graduate student experience joyous and memorable.

Most importantly, I would like to thank my parents, Vishakha and Pradeep, my elder brother, Vineet, and my grandparents for their continued warmth, blessings and support. None of this would have been possible without them.

TABLE OF CONTENTS

LIST OF TABLES

LIST OF FIGURES

SUMMARY

Polydimethylsiloxane (PDMS) is a synthetic polymer, with unique physical and chemical properties. It provides ease of fabrication for complex microscale features with tunable flexibility. This provides ample opportunity to develop PDMS microchannels with patterned microscale pillars. These pillars induce capillary wicking and with augmented pumping, provide improved heat transfer performance. In this study, the hydrodynamic and thermal performance for various PDMS micorchannel pillar assemblies has been studied for dielectric coolant FC-3283. A total of three different pillar assemblies with porosities ranging from 0.8 to 0.91 have been tested. Permeability measurements for flow rates ranging from 53 kg/m²s to 369 kg/m²s were carried out. An analytical model is developed to quantify the deformation of the PDMS channels owing to its low Young's Modulus. The single and two-phase heat transfer performance is experimentally evaluated using the same dielectric for flow rates ranging from 105 kg/m²s to 420 kg/m²s with heat fluxes ranging from 1.5 W/cm² to 16 W/cm². High-Speed Imaging is performed to study the two-phase flow characteristics. Numerical simulations have been performed to study the effects of micropillar spacing on the permeability and single-phase heat transfer coefficient. An analytical solution for single-phase laminar flow within a rectangular duct with constant heat flux input on one wall has been developed to provide a limit on the single-phase heat transfer performance of microchannels with micropillar arrays.

CHAPTER 1. INTRODUCTION

1.1 Microchannel and Micropillar Array Enhanced Heat Transfer

Microchannel heat transfer offers solutions to thermal dissipation problems for many existing and emerging applications. As the scale of devices becomes small, their thermal control and heat dissipation can be effectively accomplished through the implementation of microchannel passages [1]. The effect of channel size on the single-phase laminar heat transfer for rigid copper based rectangular microchannels has been studied previously [2]. Variable pin fin clustering on silicon based substrates has been used to dissipate heat up to 750 W/cm² using de-ionized (DI) water [3]. Flow boiling in silicon microchannels has enabled the dissipation of heat fluxes as high as 1,000 W/cm² [4]. Copper based microchannels have also presented promising results in dissipating high heat fluxes up to ~130 W/cm² [5], [6]. However, the rigid nature of silicon and copper along with their high thermal and electrical conductivity pose a difficulty in developing embedded flexible cooling systems that can isolate the system, thermally and electrically, from the ambient. This brings in the need to develop cooling technology that addresses this specific domain.

1.2 Polydimethylsiloxane (PDMS)

PDMS is a silicone elastomer most often used in microfluidic or lab-on-a-chip applications. It has a Young's Modulus ranging from 0.57 MPa to 3.7 MPa for an elastomer base to curing agent ratio ranging from 5:1 to 33:1, which gives it tunable flexibility [7]. This is significantly lower than the Young's Modulus of extensively used

materials for microchannels such as copper (~112 to 148 GPa) and silicon (~130 to180 GPa) [8], [9]. The mechanical properties of PDMS are independent of heating time for lower temperatures. The mechanical strength reduces at about 200 °C and reaches a peak at 310 °C due to thermal decomposition [10]. Furthermore, PDMS is a non-conducting polymer with an electrical conductivity of ~$4x10^{13}$ Ωm [11]. The low Young's Modulus of PDMS, coupled with its desirable thermal and electrical properties make it versatile for in-contact cooling applications for equipment with complex architecture.

1.3 Pressure drop characteristics of flexible PDMS based microchannels

The pressure drop characteristics for microchannels are vital for active and passive pumping applications. These characteristics for flexible PDMS based rectangular microchannels have been studied previously [12], [13], [14]. In these studies, an analytical model has been proposed to quantify the deformation in PDMS based flexible rectangular microchannels. Fluorescence microscopy was used to measure the deformation in PDMS microchannels with periodic circular obstacles [15], [16]. The flow characteristics for flexible PDMS microchannels are strongly dependent on microchannel deformation [17]. The flexible nature of PDMS improves the permeability of microchannels at higher flow rates as a result of the pressure build-up [18]. This unique property provides an opportunity to combine the effects of passive capillary pumping and augmented pumping. For applications with a relatively low desired flow rate, the microchannel can be used within the passive capillary pumping regime where the deformation will be relatively low and the microchannel will demonstrate rigid behavior. As the demand for the desired flow rate increases, pump system can be used. At these relatively higher flow rates, the device will perform at a higher permeability,

resulting in a lower pressure drop than a corresponding rigid microchannel. These properties make PDMS based microchannels desirable for direct in-contact cooling applications.

1.4 Convective heat transfer in PDMS microchannels

Recently, infrared thermography combined with high-speed visualizations was used to study flow boiling in PDMS microchannel with heat fluxes up to 17.92 W/cm² [19]. A hybrid rewetting mechanism was proposed to enhance the capillary-assisted evaporation/boiling in PDMS based microchannels using dielectric fluid HFE-7100, achieving a CHF of 14.7 W/cm² for a mass flow rate of 245 kg/m²s [18]. However, given the low thermal conductivity of 0.15 W/mK, the overall heat dissipation of PDMS based microchannels is limited. This brings in the need to study the effect of microchannel geometry on the overall heat transfer performance of PDMS based microchannels.

1.5 Research Objectives

Flow boiling characteristics for plain and textured surfaces with rigid SU8 micropillar arrays having a varying pitch have been previously studied [20]. This study focuses on exploring the hydrodynamic, and single and two-phase convective heat transfer performance of PDMS based flexible microchannels.

The following three cylindrical micropillar assemblies, shown in Figure 1.1, have been investigated.

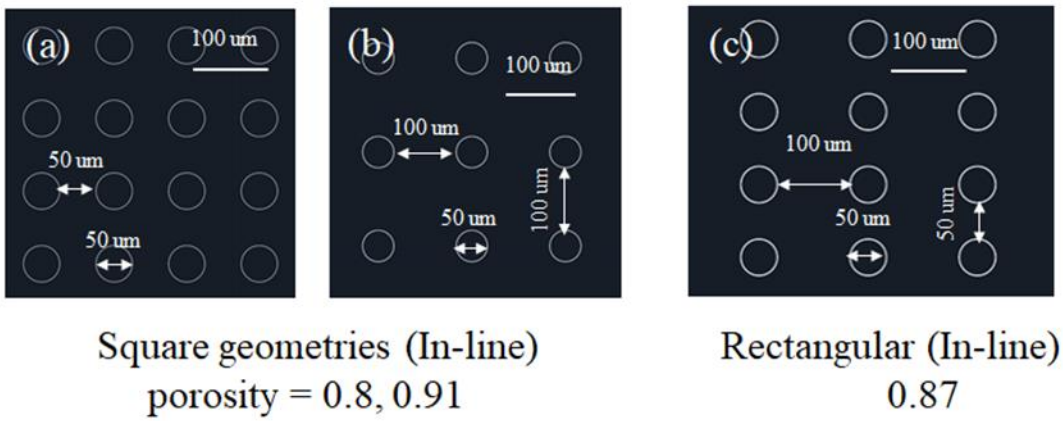

Figure 1.1: Three micropillar assemblies investigated in this study

These assemblies have a porosity varying from 0.8 to 0.91. The rectangular pillar geometry has been reported to have the best capillary performance for copper based micropillar arrays with DI-water [21]. The pillar arrangements considered in this study are designed to evaluate the effects and trade-offs of the different pillar positioning on the overall performance of the wick. The three in-line pillar arrangements help in understanding the individual effects of changes in pillar spacing in the transverse and longitudinal directions. The objectives of this study revolve around the evaluation of the overall wick performance:

- Experimentally investigate the pressure drop characteristics for forced flow ranging from 53 kg/m²s to 369 kg/m²s for the three pillar geometries.
- Develop an analytical model to estimate the deformation of PDMS microchannels with micropillar arrays under augmented pumping.

- Experimentally investigate the single and two-phase heat transfer coefficient and surface temperatures to evaluate thermal performance.
- Perform High-Speed Visualizations to understand the two-phase flow characteristics.

These four objectives provide a comprehensive investigation of the hydrodynamic and convection heat transfer performance of PDMS based flexible microchannels with patterned micropillars arrays.

CHAPTER 2. EXPERIMENTAL EVALUATION AND ANALYTICAL MODELING OF PERMEABILITY

In this chapter, the hydrodynamic performance of the three pillar geometries is experimentally evaluated through permeability measurements. The Young's Modulus of PDMS ranges from 0.57 MPa to 3.7 MPa for a mixing ratio of elastomer to the curing agent ranging from 5:1 to 33:1 which is significantly lower than that of common metals [7]. Owing to this low Young's Modulus, PDMS is highly deformable under applied pressure. An analytical model is developed and presented in this chapter to estimate the extent of the deformation caused due to forced flow.

2.1 Device Fabrication

The test section is shown in Figure 2.1 below. The PDMS wicks are fabricated through lithography in the cleanroom. A silicon mold was etched by DRIE and modified using chemical 1H,1H,2H,2H-Perfluorooctyltriethoxysilane. The PDMS mixture was then created by mixing the base elastomer and the curing agent in the ratio 10:1. The mixture was poured into the silicon mold and subsequently degassed using a desiccator. This was then cured in an oven at 100°C for two hours. Following the curing of the PDMS structure, two holes were made using a PDMS puncher to form the inlet and the outlet. The PDMS structure and the glass substrate were then bonded using oxygen plasma treatment. Two copper tubes were inserted in the two inlet and outlet holes and sealed using high-performance 3M™ Scotch-Weld™ Epoxy Adhesive DP100.

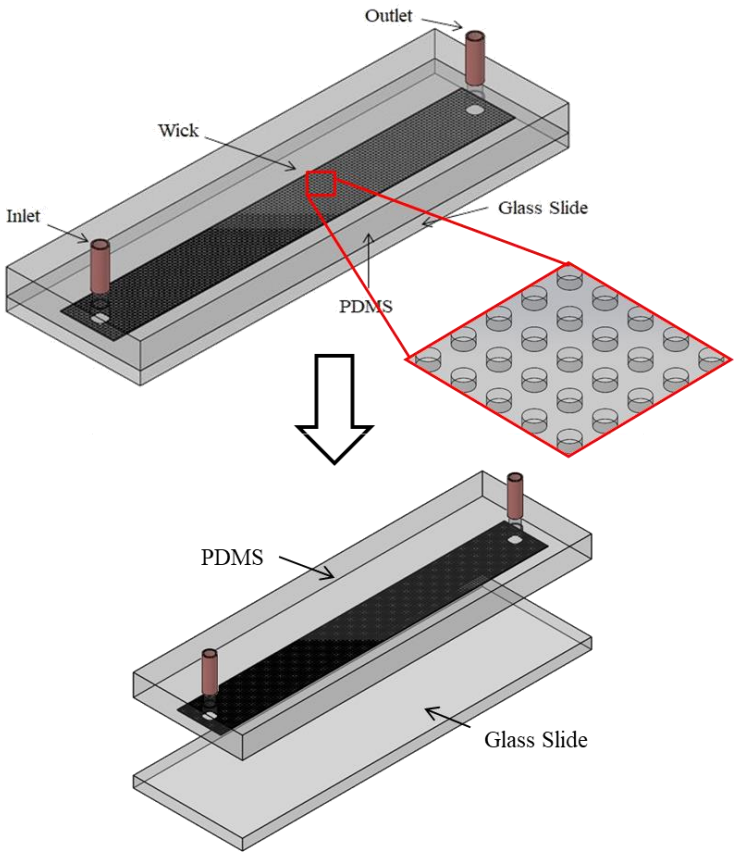

Figure 2.1: Schematic of the test device

2.2 Experimental Setup

The schematic of the closed flow-loop used for the permeability experiments is shown in Figure 2.2. A Masterflex® L/S® pump drive and a Masterflex L/S ® Easy-Load II® pump head are used to supply the fluid through the flow-loop. The flow rate is varied from 53 kg/m²s to 369 kg/m²s. A 15 µm filter is used to prevent the entry of any particulate matter into the test section. Two pressure transducers (OMEGA PX219-100A5V), one at the inlet and one at the outlet are used to measure the pressure drop across the test section. A vacuum pump (VN-200N, JB Industries Inc.) is used to vacuum the loop before each run to remove dissolved air. A total of three valves are

used to isolate different parts of the flow-loop to provide easy accessibility to the different sections. A power supply (Agilent E3649A Dual Output DC) is used to power the pressure transducers. A Data Acquisition Unit (DAQ) (Agilent 34970A) is used to log the data which is monitored using a computer. The fluid from the outlet is collected in an accumulator on an electronic weighing scale (A&D Company, Limited, HR-100AZ).

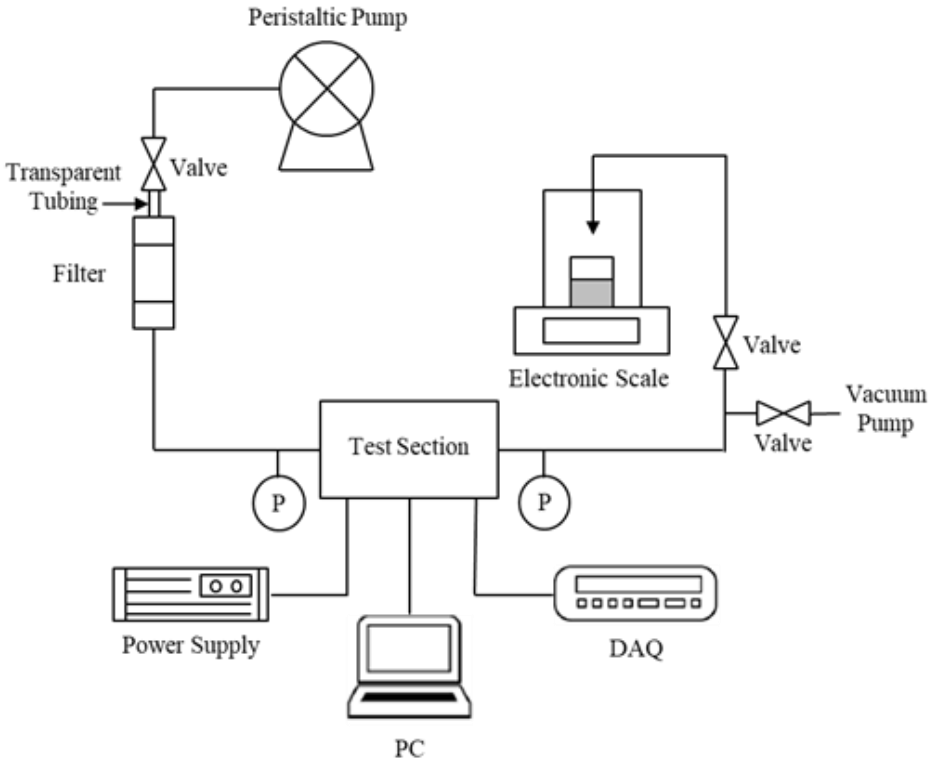

Figure 2.2: Schematic of the test setup for the permeability experiment

2.3 Uncertainty Analysis

Uncertainty analysis has been done using the method proposed by Kline and McClintock [22]. Pressure transducers were calibrated using a pressure calibrator (OMEGA DPI 610). The measurement uncertainties for flow rate, pressure, viscosity,

and microfabrication resolution are ±1%, ±1%, ±0.5%, and 3 µm. The uncertainty in the permeability has been estimated to be ±5.5%.

2.4 Results and Discussion

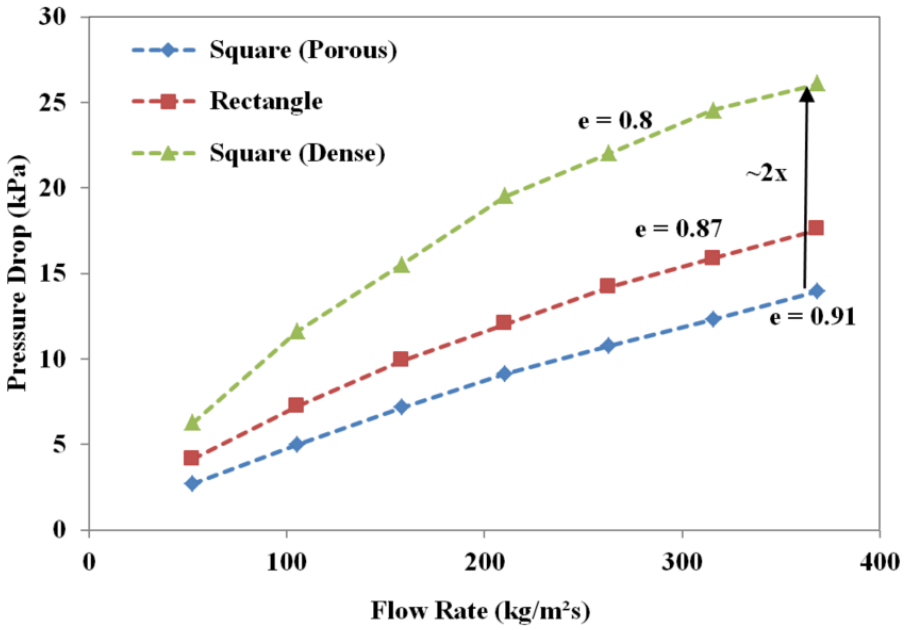

Figure 2.3: Pressure drop as a function of porosity and flow rate

Figure 2.3 compares the pressure drop for three pillar assemblies with porosities ranging from 0.8 to 0.91. The pressure drop ranges from 2.7 kPa to 14 kPa, for flow rates ranging from 53 kg/m²s to 369 kg/m²s for the Square (Porous) assembly. There is an increase in the pressure drop for geometries with lower porosity as they provide greater resistance to forced flow. A maximum pressure drop of 26.1 kPa was observed for a flow rate of 369 kg/m²s for the Square (Dense) assembly. The Reynolds number for this experiment ranges from 3.56 to 24.9. There is a ~2x increase in the pressure drop from the Square (Porous) to the Square (Dense) assembly.

The pressure drop vs flow rate relationship is linear according to Darcy's Law for Re 1~150. The non-linear Pre-Darcy flow and Post-Darcy flow regimes are observed for Re<<1 and for Re between 150~300, respectively [23]. Although the Re for the experiment lies within the laminar range, a deviation from the linear relationship was observed. As the pressure within the wick increases there is a greater deviation from the linear pressure drop-flow rate profile. This is attributed to the low Young's Modulus which results in the deformation of the channel. A maximum Darcy permeability of 817 is observed at a flow rate of 369 kg/m²s for the Square (Porous) wick.

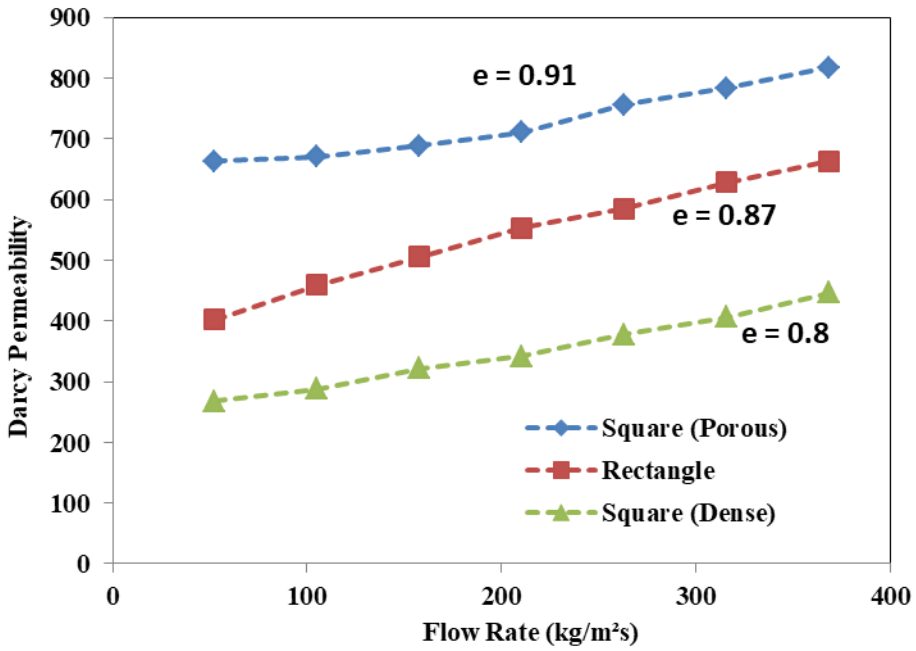

Figure 2.4: Darcy permeability as a function of flow rate

As the pressure within the wick increases with flow rate, the channel starts to deform, forming a bulge which results in the increase of the channel height and subsequently the cross-sectional area for the fluid to flow through [12]. As the cross-sectional area increases, the fluid experiences lesser resistance, which results in an

increase in the permeability. Owing to this flexible nature of the microchannel a higher permeability is observed at higher flow rates. Such a trend of increasing permeability with flow rate for a similar geometry has been previously reported [18]. An analytical model is developed and discussed to estimate this deviation and evaluate the permeability of a flexible microchannel in the next section.

2.5 Analytical Modeling of Permeability of Flexible Microchannels

The analytical evaluation of permeability for flexible microchannels is divided into two parts:

1. Estimating the deformation in a flexible channel
2. Analytical solution for permeability of micropillar arrays

In this section, the above two theories are combined to develop a solution for the permeability of flexible microchannels. In the first step, the change in the height of the channel is estimated, which subsequently results in the change in the diameter of the pillars and the overall wick porosity. The estimates of the change in these parameters are then coupled with the analytical solution for permeability of micropillar arrays. The model helps in characterizing the relative flexibility for a given channel and gives a quick solution in comparison to an intensive structural and fluid based numerical simulation.

2.5.1 Deformation Modeling

The deformation in plain rectangular flexible microchannels has been studied previously. Gervais et al coupled the laminar flow to the structural deformation through the hydrodynamic pressure exerted at the liquid-solid interface [12].

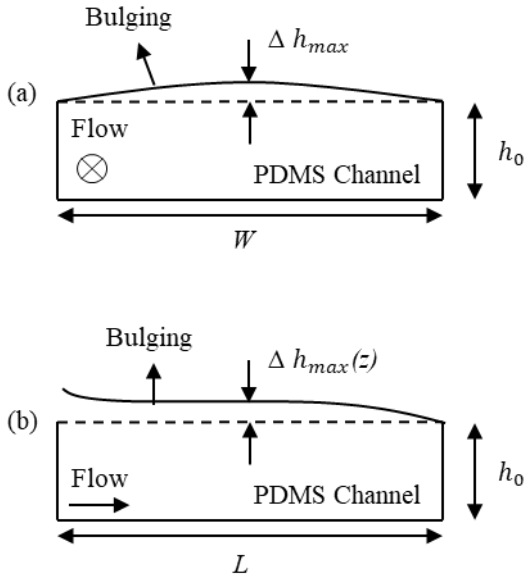

Figure 2.5: Schematic representation of the PDMS bulging effect

The schematic of this bulging effect is shown in Figure 2.5 above. For any cross-sectional area perpendicular to the direction of the flow, the top layer of the PDMS can be considered as a beam supported on both ends. The maximum bulging effect and subsequently Δh_{max} is observed at the center of this cross-section, while the channel height remains the same near the sidewalls as they are pinned to the glass surface at the bottom. As the pressure near the inlet is higher than that at the outlet, greater expansion of the channel is observed near the inlet. This effect subsides as we move along the length of the channel as the pressure gradually decreases. The expansion profile is not

perfectly linear. The bottom side bonded to the glass slide does not experience any displacement. The top side however, has a low Young's Modulus PDMS and thus undergoes deformation due to imposed pressure. This deformation is in the vertical and the lateral directions. Based on classical beam theory, the upper wall of the PDMS acts like a set of beams in parallel along the length of the flow, pinned on each side with a uniform load for a given cross-section, which changes along the length of the channel. The deformation in the vertical direction is given by [12]:

$$\in_{vertical} \sim \frac{\Delta h}{W} \sim \frac{p}{E} \tag{1}$$

where h is the height of the channel, W is the width of the channel, p is the pressure, E is the Young's Modulus.

Based on the same argument, the lateral displacement is given by:

$$\in_{lateral} \sim \frac{\Delta W}{h} \sim \frac{p}{E} \tag{2}$$

When $W >> h$ the lateral deformation can be neglected. Thus, for a rectangular channel, the change in the channel height at a given location is given by:

$$\Delta h \sim \frac{pW}{E} \tag{3}$$

The height along the length of the channel is given by:

$$h(z) = h_0\left(1 + \alpha\frac{p(z)W}{Eh_0}\right) \tag{4}$$

where h_0 is the initial height, and α is the constant of proportionality for a given channel and is on the order of 1 [12].

The model developed in this section builds on the theory previously reported. The approximations made are:

1. Weighted displacement/channel height is used for permeability computations.
2. The inlet and the outlet pressures are used to get the average pressure within the channel.

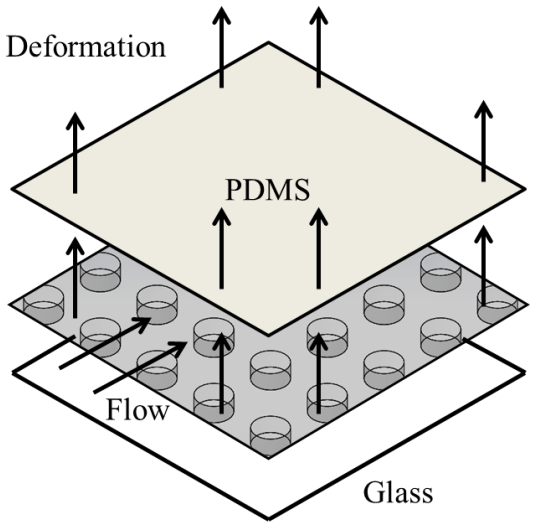

Figure 2.6: Schematic representation of the deformation effect

As shown in Figure 2.6, the wick filled with the fluid flowing through it, is sandwiched between glass on one side and flexible PDMS on the other. When the pressure builds up, this fluid exerts pressure against the PDMS and glass surfaces. PDMS having a low Young's Modulus deforms, while the glass stays as is. With this deformation in the top layer of the PDMS, three dimensional parameters change:

- Pillar height: As the top PDMS layer deforms, the micropillars which are connected to the bottom glass and the top PDMS layer expand which results in an increase in the height of the pillars. The weighted pillar height is given by:

$$h_{mean} = h_0 \left(1 + j\alpha \frac{\big(p(in) + p(out)\big)W}{Eh_0}\right) \tag{5}$$

  where *j* is the weighted average of the change in channel height, *p(in)* and *p(out)* are the inlet and outlet pressure which are evaluated experimentally.

- Pillar Diameter: With the change in the pillar height, the pillars shrink along the diameter. Using the principles of conservation of mass, the change in the diameter of the pillars is given by:

$$d_{mean} = d_0 \sqrt{\frac{h_o}{h_{mean}}} \tag{6}$$

  where $d_0$and h_0 are the original pillar diameter and height respectively.

- Porosity: The expansion of the microchannel introduces more free space within the wick increasing the porosity of the wick. This is also evident from the pressure drop measurements. The new porosity is given by:

$$\varepsilon_{new} = 1 - \frac{1 - \varepsilon_{old}}{\left(1 + j\alpha \frac{\big(p(in) + p(out)\big)W}{Eh_0}\right)} \tag{7}$$

where ε_{new} and ε_{old} are the new and the old porosity, respectively.

The above three new dimensions, namely, weighted pillar height, weighted pillar diameter, and porosity are used to evaluate the deformation in the channel.

2.5.2 Permeability Modeling

The permeability of rigid porous structures with micropillar arrays has been studied extensively. There are multiple numerical and analytical solutions that have been developed to evaluate the permeability of different pillar arrangements. Gebart et al [24] derived the permeability of regularly ordered, parallel fibers using the Navier-Stokes equations for flow along and perpendicular to the fibers. Drummond and Tahir [25] derived the solutions for the Stokes equations of motion for a viscous fluid flowing parallel and perpendicular to an array of square, rectangular, triangular and hexagonal arrays at low solid volume fraction. Tamayol et al [26] developed an analytical model for the permeability of ordered fibrous media towards normal and parallel flow. Hale et al [27] compared several models for fluid flow through square micropillar arrays to numerical simulations. In another study, Hale et al [28] reported the analytical permeability for flow through micropillar arrays with rectangular pillar arrangements.

Yazdchi et al [29] developed an analytical-numerical approach to compute the permeability of fibrous porous media. Xiao et al [30] developed a semi analytical model to predict and optimize fluid flow through micropillar arrays. Srivastava et al [31] performed a numerical simulation to compute the permeability for micropillar arrays. The results are tabulated below.

Table 1: Dimensionless permeability for square micropillar arrangement

Model	Dimensionless Permeability K* (K/d², d: pillar diameter)
Gebart et al [24] Eq. (8)	$K^*_{G,cyl} = \frac{4}{9\pi\sqrt{2}}\left(\frac{1}{2}\sqrt{\frac{\pi}{1-\varepsilon}}-1\right)^{2.5}$, ε: porosity
Drummond et al [25] Eq. (9)	$K^*_{DT,cyl} = \frac{1}{32(1-\varepsilon)}\left(ln\left(\frac{1}{1-\varepsilon}\right) - 1.476 + \frac{2(1-\varepsilon)-0.796(1-\varepsilon)^2}{1+0.489(1-\varepsilon)-1.605(1-\varepsilon)^2}\right)$
Yazdchi et al [29] Eq. (10)	$K^*_{Y,cyl} = \frac{K^s_{G2} + (K^s_D - K^s_{G2})m(\varepsilon)}{d^2}$ $K^s_{G2} = \frac{K^s_G}{1+0.336\left(\varepsilon - 1 + \frac{\pi}{4}\right)}, m(\varepsilon) = \frac{1+tanh\left(\frac{\varepsilon-0.75}{0.037}\right)}{2}$
Xiao et al [30] Eq. (11)	$K^*_{X,cyl} = K^*_{Y,cyl} + {K^*_{Y,cyl}}^{1.5}\frac{d}{h\sqrt{\varepsilon}}tanh\left(\frac{h\sqrt{\varepsilon}}{d\sqrt{K^*_{Y,cyl}}}\right)$ h: pillar height

Srivastava et al [31] Eq. (12)	$K^*_{S,cyl} = \frac{1}{30}\left(\frac{l}{h}\right)\left(\frac{h}{l-d}\right)^{1.17}\left(\frac{l}{d}-1\right)^{2.5}$ l: center − to − center pillar distance

The permeability for a rigid channel corresponding to the PDMS wick geometries was evaluated using the method proposed by Xiao et al which compared well with simulation results. The simulations were performed for a unit cell of the wick geometry as shown in Figure 2.7.

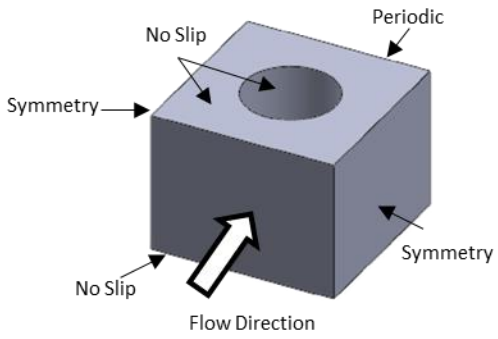

Figure 2.7 : Computational domain for pressure drop simulations

A periodic flow boundary condition was used on the two surfaces perpendicular to the direction of the flow to simulate the periodicity of the wick geometry. The two surfaces on the side were given symmetry boundary conditions as those surfaces are symmetric within the wick. The top, bottom, and the pillar surfaces were applied a no-slip boundary condition. The resultant permeabilities for the Square (Dense) and Square (Porous) assemblies are compared with the analytical solution given by Xiao et al for square micropillar arrangements. Since the permeability given by Xiao et al is just for the micropillar array, the approach reported by Hale et al [27] was used to account for

the pressure drop due to the bounding upper and lower surfaces. The approximation that the total pressure drop is equal to the sum of the individual component pressure drops, assuming a constant superficial velocity through the array was used to compute the total pressure drop within the rigid channel domain. The total non-dimensional permeability can thus be expressed as:

$$K^*_{total} = \left(\frac{1}{K^*_{cyl}} + \frac{1}{K^*_{||-plate}} \right)^{-1} \tag{13}$$

where K^*_{total} is the total non-dimensional permeability, K^*_{cyl} is the non-dimensional permeability of the micropillar array, and $K^*_{||-plate}$ is the non-dimensional permeability of a parallel plate system.

The pressure drop for a parallel plate infinite channel is given by [32]:

$$-\frac{\partial p(z)}{\partial z} = \frac{12\mu}{h^2}\, u_m \tag{14}$$

where $p(z)$ is the pressure at the stream-wise position z, h is the height of the channel, and u_m is the superficial flow velocity. Therefore, the non-dimensional permeability for a parallel plate infinite channel is given by:

$$K^*_{||-plate} = \frac{h^2 \varepsilon}{12 d^2} \tag{15}$$

where h is the height of the channel, d is the diameter of the pillars, and ε is the porosity.

The percentage error from the simulation based permeabilities for the Square (Dense) and Square (Porous) are compared with the analytical model developed by Xiao et al.

Table 2: Comparison of the simulation based permeability with the model proposed by Xiao et al

Geometry	Porosity	Simulation (μm²)	Xiao et al (2010)	% Error, Xiao
Square (Dense)	0.8	80	92	15%
Square (Porous)	0.91	168	174	3.6%

The analytical solution by Xiao et al gave an error of 15% and 3.6% in the permeability for the Square (Dense) and Square (Porous) geometries respectively. The deviation of the analytical model from the simulation based results can be attributed to the analytical model not taking into consideration the interactive effects of the parallel plates and the pillars. These results are consistent with the trends reported by Cho et al [21].

2.5.3 Semi-Analytical Solution for Permeability of Deforming Microchannels

Equations 5 - 7 are substituted into the analytical permeability solution given by Xiao et al. The permeability, inlet and outlet pressure measurements are derived from the permeability experiment.

$$h_{mean} = h_0\left(1 + j\alpha\frac{\big(p(in) + p(out)\big)W}{Eh_0}\right) \tag{16}$$

The only unknowns in this equation are j and α. However, since α, and E are constant for a given channel, we replace $\frac{\alpha}{E}$ with x. The final form of the weighted deformed channel height is given by:

$$h_{mean} = h_0 \left(1 + jx \frac{\big(p(in) + p(out)\big)W}{h_0}\right) \tag{17}$$

Equation 17 is a function of x which is the variable to be determined. Using this weighted channel height (for j = 0.6) and weighted pillar diameter the new porosity of the wick can be determined as a function of x, by substituting $\frac{\alpha}{E}$ with x, in equation 7. These equations are then substituted in equation 11 and solved in MATLAB to determine the value of x.

Figure 2.8 shows the x value as a function of the flow rate. At relatively lower flow rates, the capillary forces are dominant which improve the permeability of the wick. The experimentally measured permeability is higher than the one predicted by the Xiao model and numerical simulations. This is due to the capillary effects which are not accounted for in the Xiao model. This is reflected in the higher x value at relatively lower flow rates which subsequently flattens out as the forced flow effects start to dominate the capillary effects. Therefore, the initial values of x are not an accurate representation of the deformability of the wick. As the flow rate increases and the forced flow effects start to dominate the overall hydrodynamic performance of the wick, an average x value of 0.362 MPa^{-1} and 0.252 MPa^{-1} is observed for the Square (Porous) and the Square (Dense) pillar assemblies, respectively. A deviation of ±5% and ±2% was observed in the x value for the Square (Porous) and Square (Dense) geometries

respectively. A higher value of x suggests that the channel is more susceptible to deformation under similar pressure conditions. In this case, the more porous geometry has an x value ~1.5 times that of the denser geometry.

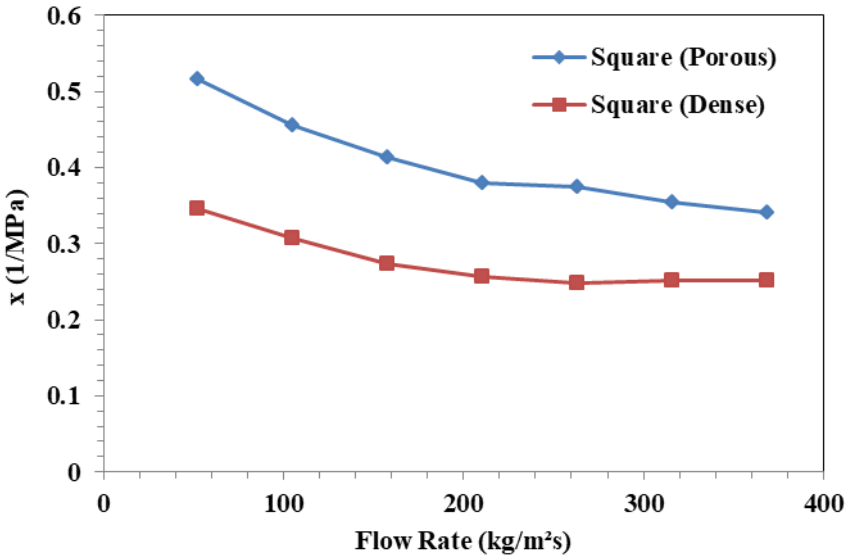

Figure 2.8: $x\left(\frac{\alpha}{E}\right)$ value for j = 0.6

The pillars within the wick are bonded to the glass slide and stem from the PDMS base. These pillars act as primary elastic resistors that resist the deformation in these channels. As the number of pillars increases, there is an increase in the resistance to deformation. This can very well be observed for the two pillar geometries being considered in this study. The denser geometry with a porosity of 0.8 has ~2.25 times the number of pillars than the porous geometry with a porosity of 0.91. The higher number of pillars ensures that the denser geometry doesn't deform as much as the porous geometry under similar pressure conditions. There are a number of ways in which 'α' and the Young's Modulus of these wicks can be altered. 'α' can be altered by changing the pillar arrangement, pillar diameter, pillar spacing and pillar geometry. The Young's

Modulus of PDMS can be altered by changing the mixing ratio of the PDMS base and the curing agent, and the curing temperature and time [7]. By changing these parameters, the deformability of the channel can be manipulated to achieve a desired level of flexibility for the channel.

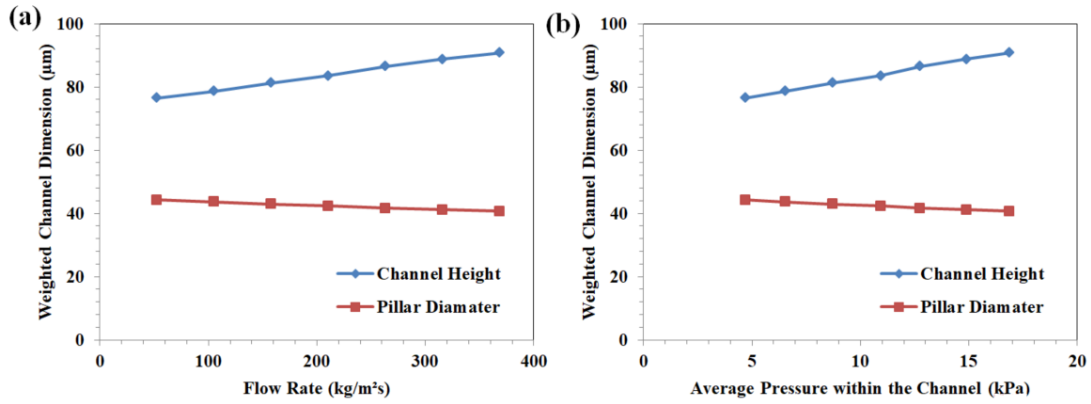

Figure 2.9: Variation in the channel height and pillar diameter for the Square (Porous) assembly as a function of (a) Mass Flow Rate (b) Average Pressure within the Channel

Figure 2.9 shows the variation, given by the analytical solution, in the average channel height and the pillar diameter as a function of the mass flow rate and the average pressure within the channel. As the mass flow rate increases, the average pressure within the channel increases. This increase results in an increase in the average channel height and a decrease in the average pillar diameter. Numerical simulations were performed using the estimated channel height and pillar diameter, for the deformed channel. These simulations were performed for a unit cell of the wick geometry as shown in Figure 2.7.

Figure 2.10 compares the pressure drop as a function of the mass flow rate for:

- Experimental Data
- Simulation results for a rigid microchannel corresponding to the fabricated flexible microchannel dimensions
- Simulation results for channel dimensions given by the analytical solution

The deviation in the pressure drop characteristics, from a rigid channel, is consistent with previous studies [12]- [15], [17]. The simulations performed based on the results provided by the analytical solution have a minimum, maximum, and average deviation from the experimental data, of 5.2%, 15.7%, and 10.1%, respectively.

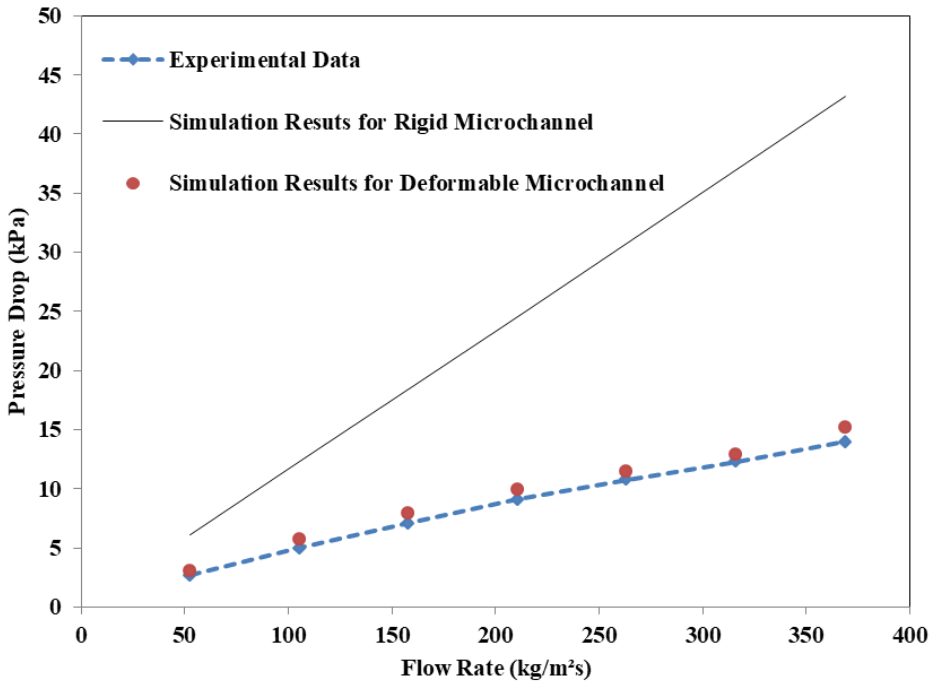

Figure 2.10: Comparison between simulation results for a rigid microchannel, deformable microchannel and corresponding experimental results for a flexible PDMS microchannel

CHAPTER 3. EXPERIMENTAL AND ANALYTICAL INVESTIGATION OF SINGLE AND TWO-PHASE CONVECTION IN PDMS MICROCHANNELS

In this chapter, the single and two-phase convective heat transfer performance of the three pillar geometries is experimentally evaluated and discussed. The objective of these experiments is to evaluate the single and two-phase heat transfer coefficient and the corresponding wall temperature. The dielectric fluid FC-3283 with an atmospheric pressure boiling point of 128°C is used for these experiments. High-Speed Imaging is employed to understand the two-phase flow characteristics. These results show a steady transition from isolated slug flow to combined bubble nucleation, coalescence and slug formation followed by vigorous two-phase as the heat flux increases. These experiments are performed for a mass flow rate ranging from 105 kg/m²s to 420 kg/m²s.

An analytical solution, validated by simulations, has been used to provide the limiting case scenario for laminar flow single-phase heat transfer in micropillar array based rigid microchannels. The single phase convective heat transfer performance has been compared with the pressure drop characteristics of these geometries to provide a trade-off study between the hydrodynamic and single-phase convective heat transfer performance.

3.1 Test Section

The PDMS wicks are fabricated through lithography in the cleanroom. A silicon mold was etched by deep reactive ion etching (DRIE) and modified using chemical

1H,1H,2H,2H-Perfluorooctyltriethoxysilane. The PDMS mixture was then created by mixing the base elastomer and the curing agent in the ratio 10:1. The mixture was poured into the silicon mold and subsequently degassed using a desiccator. This was then cured in an oven at 100°C for two hours. Following the curing of the PDMS structure, two holes were made using a PDMS puncher to form the inlet and the outlet. An aluminum serpentine heater was printed on a glass surface to act as the heat source. It was fabricated and provided by Dr. Wenming Li, postdoctoral fellow at the Microelectronics and Emerging Technologies Thermal Lab in the Department of Mechanical Engineering at Georgia Tech. The heater electrical resistance as a function of temperature was determined by recording the resistance to temperature relationship during a slow cooldown process in an oven, with closed doors. This ensured slow temperature decay (~10 hours) to determine the resistance to heater temperature relationship. A linear fit was used to estimate the heater surface temperatures during the experiments. The PDMS structure and the glass substrate with the heater were then bonded using oxygen plasma treatment. Two copper tubes were inserted in the two inlet and outlet holes and sealed using 3M™ Scotch-Weld™ Epoxy Adhesive DP100.

3.2 Experimental Setup

The schematic of the open-loop test setup used for the single and two-phase convective heat transfer experiment is shown in Figure 3.1. Chemyx Nexus 6000 syringe pump is used to supply the fluid to the test section. The working fluid is degassed prior to the tests. The mass fluxes for this experiment range from 105 kg/m²s to 420 kg/m²s. A 15 um filter is used to prevent particulate impurities from entering the test section. Two pressure transducers (OMEGA PX219-100A5V) and T-type thermocouples (OMEGA

Immersion Probe 1.5mm diameter), one at the inlet and one at the outlet, are used to measure the pressure drop and temperature, respectively, across the test section. A vacuum pump (VN-200N, JB Industries Inc.) is used to vacuum the loop before each run to remove dissolved air. A power supply (Agilent E3649A) is used to power the pressure transducers and the aluminum printed heater. Data Acquisition Unit (Agilent 34970A) is used to log the data which is monitored using a computer. The fluid from the outlet is collected in an accumulator on an electronic weighing scale (A&D Company, Limited, HR-100AZ).

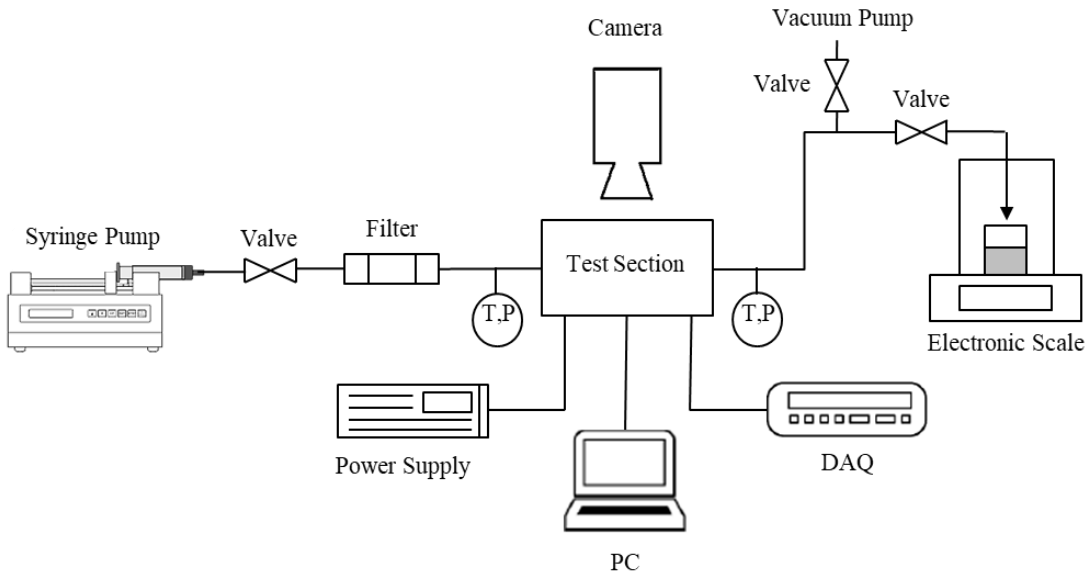

Figure 3.1: Schematic of the open-loop test setup for thermal performance testing

3.3 Uncertainty Analysis

Uncertainty analysis has been done using the method proposed by Kline and McClintock [22]. The measurement uncertainties for flow rate, voltage, current, temperature, and microfabrication resolution are ±1%, ±1%, ±1%, ±0.5 °C, and 3 μm.

The uncertainties in the effective heat flux, single-phase and two-phase heat transfer coefficient have been estimated to be ±2%, ±11.2%, and 9.8% respectively.

3.4 Results and Discussion

The effective heat flux for these experiments ranges from 1.5 W/cm² to 16 W/cm² for a flow rate ranging from 105 kg/m²s to 420 kg/m²s. A heat loss experiment was performed to estimate the heat loss from the heater to the test section and the ambient. This was deducted from the total input power to evaluate the effective heat input. The average surface temperature of the wall was estimated using 1-D conduction through the glass layer. The computations are given below.

$$q''_{total} = VI/A \tag{18}$$

$$q''_{eff} = q''_{total} - q''_{loss} \tag{19}$$

$$\bar{T}_{heater} = \bar{T}_0 + k(R - R_0) \tag{20}$$

$$\bar{T}_{wall} = \bar{T}_{heater} - q''_{eff} t_p / k_p \tag{21}$$

where R_0 is the resistance of the heater at ambient temperature, R is the resistance of the heater at the corresponding input power, t_p is the thickness of the pyrex layer and k_p is the thermal conductivity of the fluid.

The heat transfer coefficient is given by:

$$h_{overall,single-phase} = \frac{q''_{eff}}{\left(\bar{T}_{wall} - \frac{T_{in} + T_{out}}{2}\right)} \tag{22}$$

$$h_{overall,two-phase} = \frac{q''_{eff}}{(\bar{T}_{wall} - T_{sat})} \tag{23}$$

3.4.1 Test Setup Limitations

The testing of high boiling point fluids in this setup has the following limitations:

- The maximum allowable temperature beyond which PDMS can sustain mechanical damage is 200 °C [10].
- The lower thermal conductivity of pyrex (1.005 W/mK) results in a temperature gradient of 4.67°C per unit power input.
- The maximum allowable temperature for the aluminum heater is ~250°C.
- The single-phase to two-phase transition data is limited as the heater does not have point control for temperature measurements. During the initial stages of boiling, it is observed that the average wall temperature is below T_{sat}. However, the relatively higher wall temperatures near the outlet result in the onset of nucleate boiling, while the bulk of the fluid is not boiling. Therefore, using T_{sat} as the fluid temperature is not an accurate representation of the heat transfer coefficient as the bulk of the fluid, during the initial stages of boiling, is still below T_{sat}.

Figure 3.2: Heater damage due to high temperature operation

Figure 3.2 shows the damage observed along the serpentine heater with a magnified view showing the heater getting cut off due to prolonged high temperature use. The maximum allowable temperature for PDMS and the heater, coupled with the temperature gradient across the glass limits the testing for high boiling point fluids. The experiments were limited to a maximum temperature of ~170 °C for the surface which is in direct contact with PDMS.

3.4.2 Single and Two-Phase convective heat transfer characteristics

The results for the heat transfer coefficient at two different flow rates of 210 kg/m²s and 420 kg/m²s for the Square (Dense) geometry are shown in Figure 3.3. The flow is within the laminar regime with Re between 14.1~28.2. The heat transfer coefficient increases with increase in heat flux as the flow transitions from single-phase to two-phase. The sudden increase in the heat transfer coefficient at 6.4 W/cm² and 9.9 W/cm² for the two flow rates marks the onset of nucleate boiling with isolated bubbles observed near the outlet. The higher heat flux for the onset of nucleate boiling at a relatively higher flow rate is attributed to efficient wetting of the surface. There is a sharp increase in the heat transfer coefficient during two-phase. Within the nucleate

boiling regime, at relatively lower heat fluxes, a higher heat transfer coefficient is observed which is consistent with the results reported by Li et al. [18].

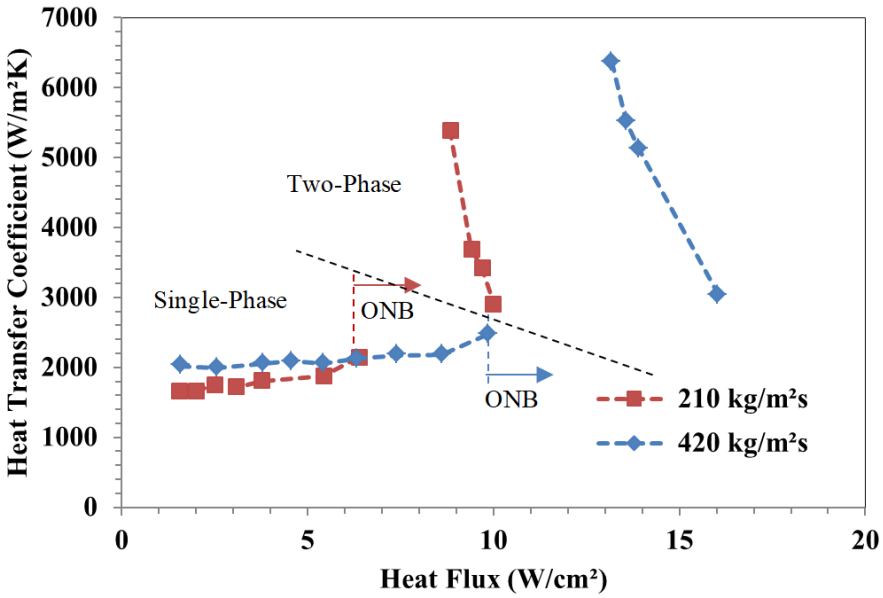

Figure 3.3: Overall heat transfer coefficient versus heat flux

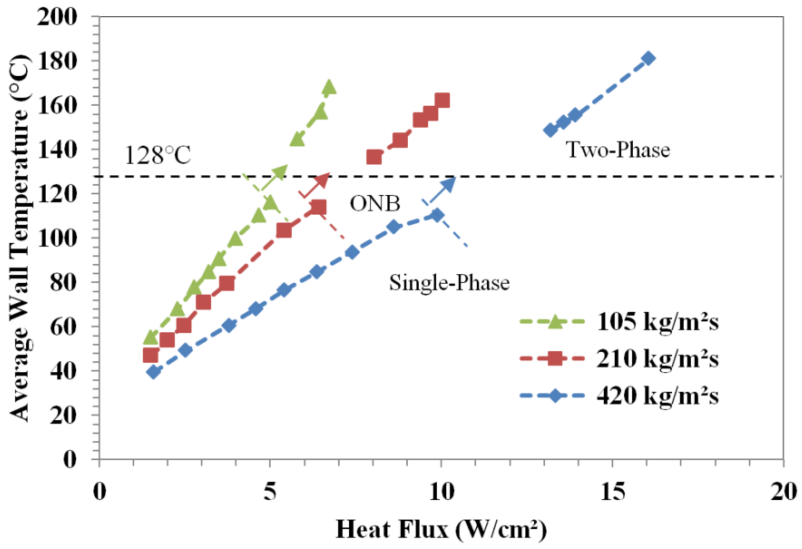

Figure 3.4: Average wall temperature as a function of heat flux

Figure 3.4 shows the variation in the average wall temperature as a function of the heat flux for three different flow rates. The onset of nucleate boiling can be observed with a change in the slope of the average wall temperature curve. A higher flow rate ensures a lower average wall temperature at the same heat input. The rate of change of wall temperature with respect to the heat flux is higher at lower flow rates.

3.4.3 High-Speed Visualizations

High-Speed Imaging was performed to study the two-phase flow characteristics within the microchannel. A Phantom V211 (Vision Research, Inc.) was used to perform the high-speed visualizations at 2,200 frames per second (fps). The recorded high-speed videos were post-processed using the PCC 3.4 software provided by the same company.

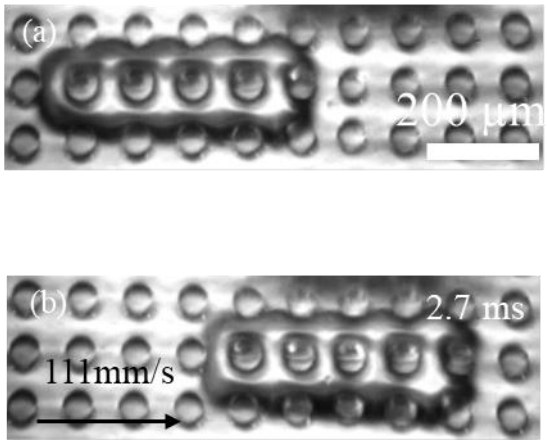

Figure 3.5: Slug flow; HF = 6.9 W/cm², FR = 210 kg/m²s

Figure 3.5 shows the two-phase slug flow observed at a heat flux of 6.9 W/cm² for a flow rate of 210 kg/m²s. These slugs were observed near the walls of the microchannel where the velocity of the fluid was relatively lower than the bulk region. The slug was observed to be moving at 111mm/s for a flow rate corresponding to a

superficial velocity of 116 mm/s. It can be observed that the vapor does not propagate in a direction perpendicular to the flow given the high pressure stagnation zones which are generated behind the pillars.

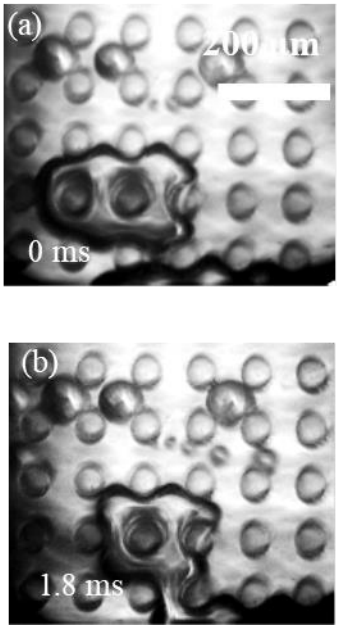

Figure 3.6: Bubble nucleation, coalescence and slug formation; HF = 8.5 W/cm², FR = 210 kg/m²s

Figure 3.6 shows bubble nucleation, coalescence and slug formation for a heat flux of 8.5 W/cm² for a flow rate of 210 kg/m²s. As the heat flux increases, the effect of nucleate boiling on the two-phase flow characteristics is more profound. The surface roughness and stagnation zones promote bubble nucleation. The bubbles are drawn into the free flow channel between the pillars given the lower pressure. These bubbles undergo coalescence to form larger slugs. Figure 3.7 captures the effect of bubble nucleation and subsequent slug formation.

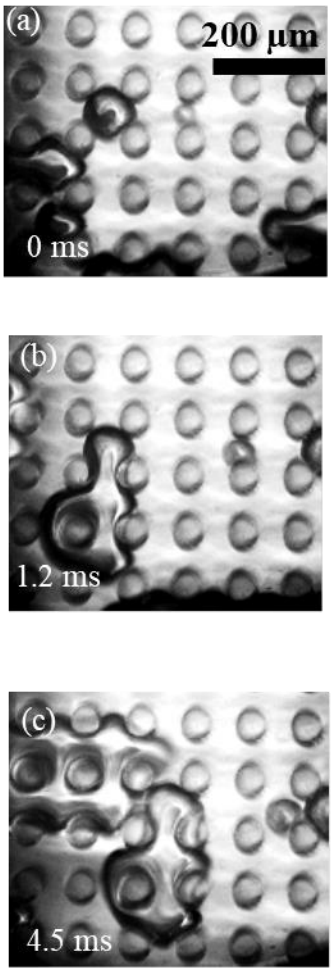

Figure 3.7: Bubble nucleation and slug formation; HF = 8.5 W/cm², FR = 210 kg/m²s

As the heat flux is increased further, vigorous two-phase flow is observed near the walls of the wick. Given the lower velocity of the fluid near the side walls of the wick, a vapor film is formed which propagates further into the bulk region as the heat flux is increased. As shown in Figure 3.8, a vapor film is formed near the side wall while large slugs were observed to be flowing through the bulk of the fluid. This vapor film propagates towards the liquid region as the heat flux is increased.

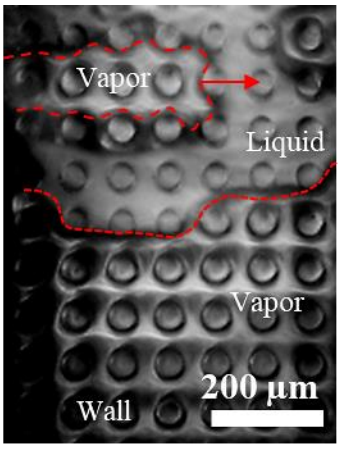

Figure 3.8: Vapor film observed near the side wall; HF = 9.1 W/cm², FR = 210 kg/m²s

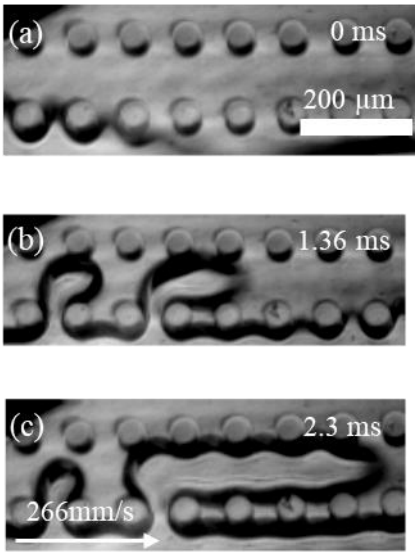

Figure 3.9: Vapor removal mechanism; HF = 4.78 W/cm², FR = 63 kg/m²s

Figure 3.9 above shows the vapor removal mechanism at a heat flux of 4.78 W/cm² for a relatively low flow rate of 63 kg/m²s. The vapor can be seen making its way into a parallel channel with a velocity of ~266mm/s. This is significantly higher than the superficial velocity of 58 mm/s. This increase in the local flow velocity improves the overall convective heat transfer performance. The introduction of a vapor flow pathway

suggested by Li et al [18] can further improve the vapor removal process reducing local hotspots and promoting rewetting of the surface.

As shown in Figure 3.10 below, vapor backflow was observed at an extremely low flow rate of 21 kg/m²s. The vapor can be seen propagating in a direction opposite and perpendicular to the flow. The rapid bubble growth overcomes the imposed mass flow rate to create a backflow which results in temperature and pressure instabilities.

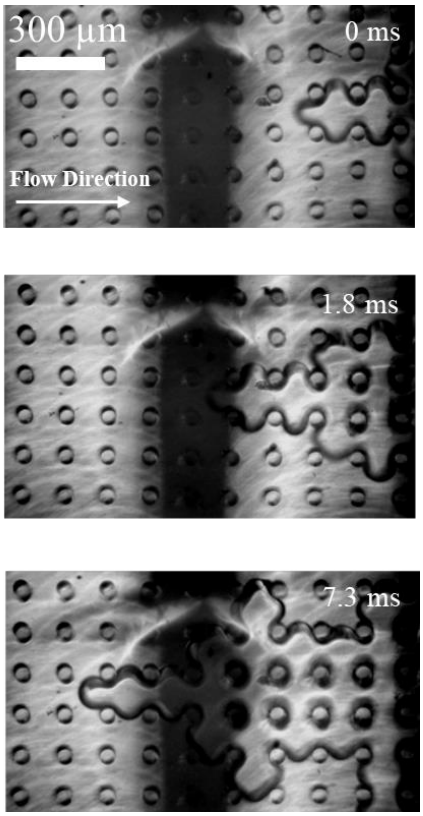

Figure 3.10: Vapor backflow; HF = 2.3 W/cm², FR = 21 kg/m²s

3.4.4 Single-Phase convective heat transfer performance comparison

Figure 3.11 below shows the variation in the average wall temperature as a function of heat flux for the three pillar assemblies for single-phase flow. The Square

(Dense) wick gives the lowest average wall temperature as a function of heat flux. The average wall temperature at a given heat flux increases with increase in porosity. Decreasing the porosity of the wick results in an increase in the mixing of the fluid which promotes lower average wall temperatures and higher heat transfer coefficients. Furthermore, this improvement in the mixing delays the onset of nucleate boiling.

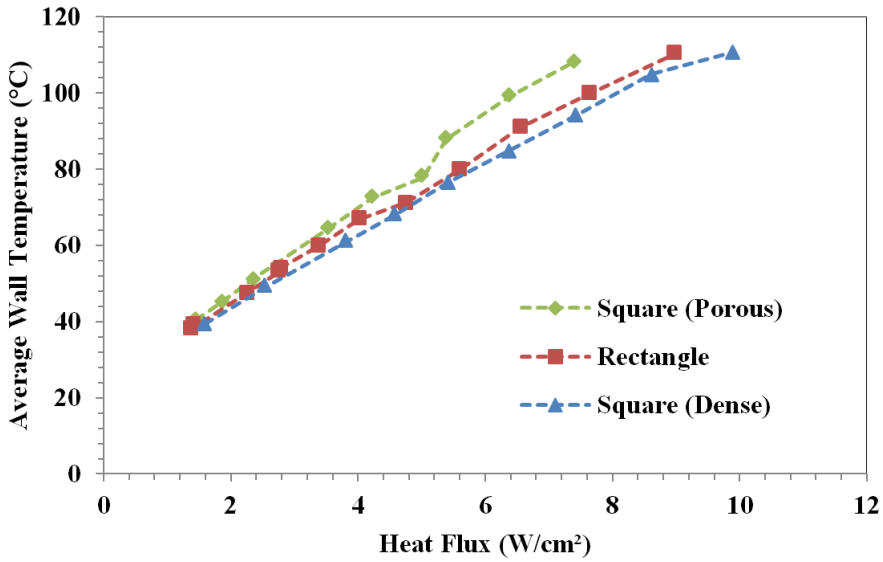

Figure 3.11: Single-phase average wall temperature for the three pillar assemblies at a flow rate of 420 kg/m²s

Figure 3.12 shows the overall single phase heat transfer coefficient for the three geometries as a function of heat flux for a flow rate of 420 kg/m²s. An average single-phase heat transfer coefficient of 2,133 W/m²C, 1,833 W/m²C, and 1,532 W/m²C was observed for the Square (Dense), Rectangular, and Square (Porous) pillar geometries. A 39% and 20% increase in the single-phase convective heat transfer performance was observed for the Square (Dense) and Rectangular pillar geometries, respectively, as compared to the Square (Porous) geometry. The onset of nucleate boiling is marked by

the increase in the heat transfer coefficient. Although the average temperatures corresponding to the onset of nucleate boiling are lower than T_{sat}, two-phase flow is observed through isolated bubbles near the outlet where the surface temperature is higher than T_{sat}.

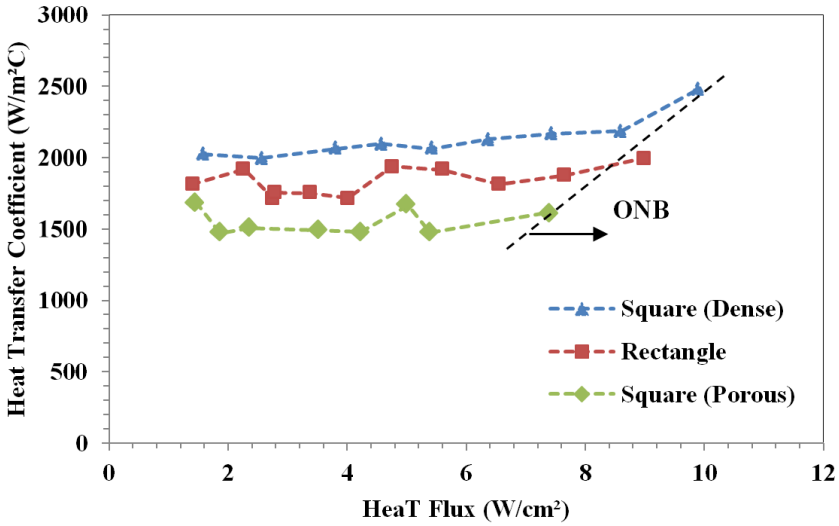

Figure 3.12: Single-phase heat transfer coefficient for the three pillar assemblies at a flow rate of 420 kg/m²s

Table 3 provides a comprehensive comparison of the single-phase thermal performance of copper, silicon, and PDMS based microchannels with working fluids having similar properties as FC-3283.

Table 3: Comparison of single-phase thermal performance of Copper/Silicon/PDMS based devices with present study

Reference	Number of Channels and Geometry	Channel Dimensions (H, W, L)	Hydraulic Diameter	Substrate Material	Coolant	Total Mass Flux (kg/m^2s)	Maximum Single-Phase Operation Heat Flux (W/cm^2)	Overall HTC (kW/m^2K)
Chen et al (2005) [33]	Ten Parallel Channels	2.5 mm, 504 µm, 25.4 mm	840	Copper	FC-77	706 ~ 1180	~1.2	~0.53
Haricharan et al (2008) [34]	Multiple Parallel Channels	650 µm, 100~5850 µm, 12.7 mm	173 - 1170	Silicon	FC-77	250 ~ 1600	2~7.3	0.75~1.92
Yang et al(2014) [35]	Five Parallel Channels with Herringbone Mixers	250 µm, 220 µm, 10 mm	234	Silicon	HFE-7000	1018 ~ 2206	16~30	8~11.2
Li et al (2020) [18]	Micropillar Assembly with Vapor Pathways	70 µm, 25/100µm, 20 mm	37/83.7	PDMS	HFE-7100	70~245	1.2~3.5	N/A
Present Study	Micropillar Assembly	60 µm, 50-100 µm, 25 mm	55-75	PDMS	FC-3283	210~420	1.5~8.6	1.5~2.1

3.4.5 Two-Phase convective heat transfer performance comparison

Figure 3.13 compares the average wall temperature as a function of the heat flux for the Square (Dense) and the Rectangular pillar geometries for two flow rates of 210 kg/m²s and 420 kg/m²s. The average wall temperature for a given heat flux is higher for the Rectangular pillar geometry as compared to the Square (Dense) pillar geometry. Figure 3.14 shows the corresponding heat transfer coefficient for single and two-phase convective heat transfer for the Square (Dense) and the Rectangular pillar geometry as a function of heat flux for a flow rate of 420 kg/m²s. The heat transfer coefficient is higher for the Square (Dense) pillar geometry as compared to the Rectangular pillar geometry.

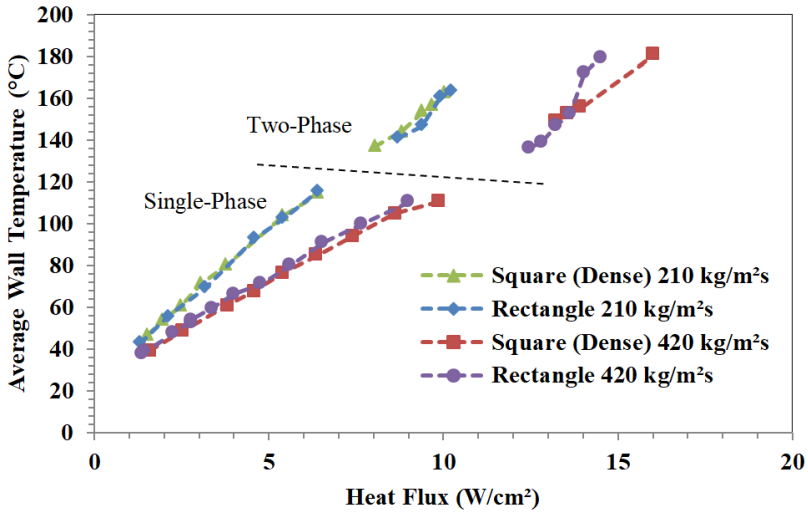

Figure 3.13: Comparison of average wall temperature as a function of the heat flux for Square (Dense) and Rectangular pillar assemblies

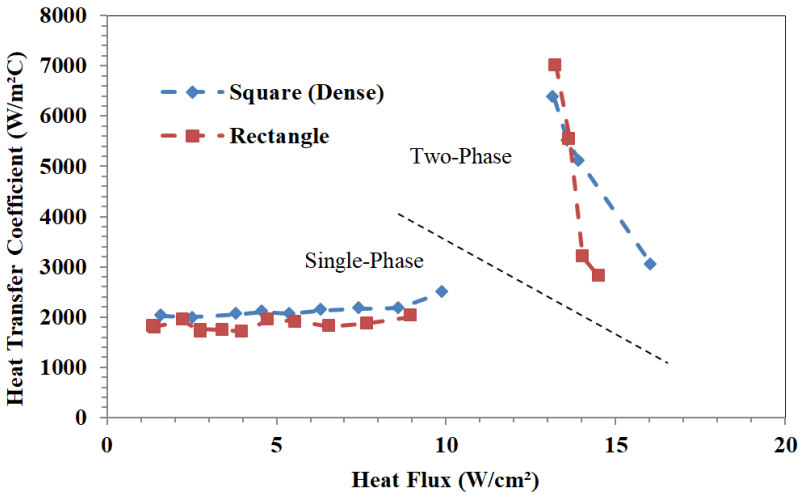

Figure 3.14: Heat transfer coefficient as a function of heat flux for the Square (Dense) and Rectangular pillar assemblies

3.4.6 Overall Single-Phase Wick Performance Evaluation

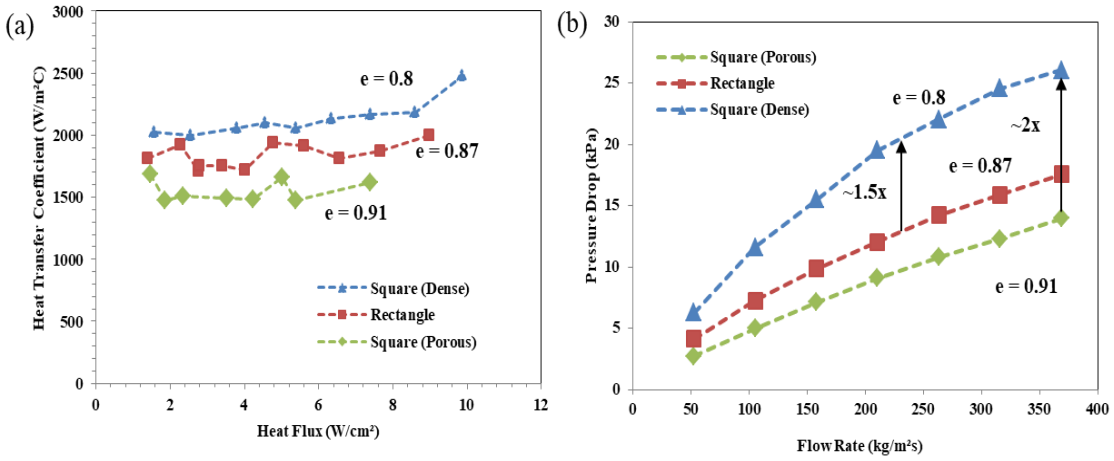

Figure 3.15: Overall Performance of the Microfluidic Device: (a) Single-phase heat transfer coefficient as a function of heat flux for the three pillar assemblies at a flow rate of 420 kg/m²s; (b) Pressure Drop as a function of the flow rate for the three pillar assemblies.

Figure 3.15 (a) and (b) compares the overall single-phase convective heat transfer and hydrodynamic performance of the three pillar assemblies. The Square (Dense) pillar

geometry provides the best single-phase heat transfer performance, while the Square (Porous) pillar geometry provides the best hydrodynamic performance. Compared to the Square (Porous) geometry, an increase of 39% and 20% in the single-phase heat transfer coefficient is observed for the Square (Dense) and Rectangular pillar geometry, respectively. Similarly, compared to the Square (Dense) geometry, an increase of 83% and 48% in the hydrodynamic performance is observed for the Square (Porous) and Rectangular pillar geometry, respectively.

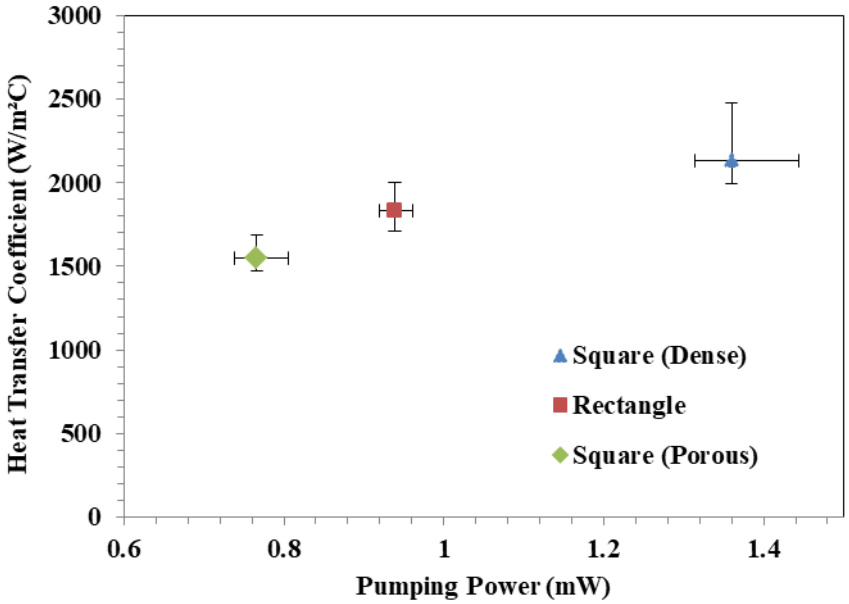

Figure 3.16: Average HTC as a function of the Pumping Power, G = 420 kg/m²s

Figure 3.16 shows the average single-phase heat transfer coefficient as a function of the pumping power for the three different geometries at a mass flow rate of 420 kg/m²s. An increase of ~38% is observed in the single-phase heat transfer coefficient at the expense of an increase of ~78% in the pumping power as the porosity is decreased from 0.91 to 0.8. From these results, it can be established that the effect of pillar spacing

is more profound on the hydrodynamic performance than the single-phase heat transfer coefficient.

3.5 Recommendations for Overall Microchannel Performance Enhancement

The thermal performance of plain surfaces can be enhanced through surface modifications. Parallel microchannels and micropillar array based geometries provide a larger surface area, as compared to a plain surface, resulting in more nucleation sites and larger heat dissipation area which improve the thermal performance. As compared to PDMS based parallel microchannels, PDMS based microchannels with micropillar arrays have been shown to prevent hotspots and dryout through timely rewetting [18]. While designing cooling devices with micropillars, two physical parameters need to be considered – permeability and heat transfer coefficient. For any cooling device, the goal is to achieve the highest possible permeability and heat transfer coefficient. As seen from this study, for the geometry considered, increase in the porosity results in an increase in the permeability and a decrease in the heat transfer coefficient. Therefore, for the design of these surface modifications, it is imperative to understand the simultaneous effects of these two parameters.

For the design of microchannels with micropillar arrays, there are three major design parameters – pillar shape, pillar dimensions, and pillar spacing. This study focuses on studying the effects of pillar spacing on the overall microchannel performance. For microchannels with cylindrical micropillars, as seen in Figure 3.16, decreasing the porosity from 0.91 to 0.8, results in an increase of ~38% in the single-phase heat transfer coefficient for a corresponding increase of ~78% in the pumping

power. Similarly, by decreasing the porosity from 0.87 to 0.8, there is an increase of ~16% in the single-phase heat transfer coefficient for a corresponding increase of ~45% in the pumping power. It can be concluded that, the effect of porosity/pillar spacing on the pumping power is more significant than that on the single-phase heat transfer coefficient. Furthermore, lower porosity/pillar spacing results in a higher capillary pressure resulting in a better prevention of dryout as compared to a relatively more porous configuration. As reported by Bigham et al [20], a reduction in the pillar spacing from 50 μm to 20 μm resulted in an increase in the heat transfer coefficient and the critical heat flux, which was attributed to an increase in the capillary pressure. However, a further decrease from 20 μm to 10 μm pillar spacing resulted in a decrease in the heat transfer coefficient and the critical heat flux.

Zhou et al [36] experimentally and numerically investigated heat transfer enhancement for different shapes of micro pillars embedded in copper based microchannel heat exchangers. The five different micropillar cross-sectional shapes studied included – square, circle, fan-shape, drop-shape, and irregular drop-shape. The hydrodynamic performance, in terms of pressure drop and friction factor, of the drop-shape and the irregular drop-shape was shown to be ~35% higher than the other three geometries. The Nusselt number for the two drop-shaped geometries was ~5% lower than the other three geometries. Ranjan et al [37] studied the wicking and thermal characteristics of different copper based micropillar structures for use in passive heat spreaders. It was reported that the cylindrical micropillar geometry had the highest capillary pressure, as compared to conical and pyramidal shaped micropillars, for contact angles between 5°~60°. It was also reported that the conical and pyramidal

shaped micropillars had a larger thin-film area and a higher permeability, as compared to cylindrical micropillars, for contact angles between 5°~60°. However, given the lower thermal conductivity of PDMS as compared to Copper/Silicon, the thin-film evaporation effect is not as profound while the capillary pressure and permeability effects remain similar.

From a practical design standpoint, the reliability of these devices is extremely crucial. PDMS based devices are stated to function nominally up to an operational temperature of ~200°C. In this study, a maximum temperature of ~180°C damaged the heater, as shown in Figure 3.2, but no visible damage was observed on the PDMS structure. Given the higher CHF for a lower pillar spacing [20], for reliable operation, it is optimal to use a lower pillar spacing, to prevent any hotspots and dryout for a given mass flow rate. However, this comes at the cost of a lower permeability and higher pumping power requirement.

In many applications, the heat dissipation is not uniform. To address the heat dissipation at local hotspots, a more densely packed micropillar assembly can be implemented locally. This will ensure a higher heat transfer coefficient locally, which will result in a uniform temperature distribution throughout the entire heat dissipating area. The densely packed micropillar region will also enhance capillary effects which will prevent dryout at higher heat fluxes. Furthermore, increasing the micropillar density locally, and not throughout the entire microchannel, will ensure a lower pressure drop while meeting the requirements of hotspot mitigation.

The flexible nature of PDMS provides an opportunity to develop cooling apparatus for flexible and wearable electronics. This study focuses on the effects of using a flexible material for developing active cooling devices. One of the key focuses of this study was to understand and quantify the susceptibility to deformation for PDMS based microchannels with micropillar arrays. It was concluded that, a porous microchannel is more susceptible to deformation than a densely packed microchannel. A more flexible PDMS microchannel will be more compliant for flexible applications, but will also deform more under pressure. There are a number of ways in which the susceptibility to deformation of these microchannels can be altered as it depends on physical parameters like - pillar arrangement, pillar dimensions, pillar spacing and pillar geometry. The Young's Modulus of PDMS can be altered by changing the mixing ratio of the PDMS base and the curing agent, and the curing temperature and time. By changing these parameters, the deformability of the channel can be manipulated to achieve a desired level of flexibility for the channel.

To develop a PDMS based cooling device the major design parameters include –

1. Micropillar Assembly - The three design parameters for a micropillar assembly are:
    a. Pillar Shape: Various pillar shapes can be used based on the operational requirements. The pillar shapes have a significant impact on the capillary pressure and permeability [36], [37]. A higher capillary pressure ensures timely rewetting, preventing dryout. A higher permeability ensures a lower pressure drop against forced flow. Capillary pressure and permeability are competing effects.

b. Pillar Dimensions and Spacing: Pillar spacing affects the capillary pressure and permeability. A relatively higher pillar spacing, for a given pillar shape, results in a relatively lower capillary pressure and higher permeability.

c. Pillar Arrangement: The pillars can be arranged in an in-line or staggered pattern. It has been previously reported that the capillary performance of the in-line rectangular pillar arrangement is optimal [21].

2. Working Fluid - The fluid-solid contact angle is an important factor affecting the capillary pressure. A lower contact angle results in a higher capillary pressure. Also, as the HTC for two-phase flow is higher than that of single-phase flow, it is optimal to operate within the two-phase regime. Therefore, the working fluid can be determined based on the maximum operational wall temperature requirement (limited to <~200°C), such that the device works within the two-phase regime.

3. Deformability of the channel - The deformability of the channel can be fine-tuned as per the flexibility requirements based on – microchannel porosity, PDMS base to curing agent mixing ratio, and PDMS curing time and temperature.

    a. Microchannel Porosity: A porous microchannel is more deformable than a densely packed microchannel.

    b. PDMS base to curing agent mixing ratio: A higher mixing ratio results in a lower Young's Modulus making the structure more flexible/susceptible to deformation.

c. PDMS curing time and temperature: A higher curing time and temperature result in a higher Young's Modulus making the structure less flexible/susceptible to deformation.

This study reports the effects of different design parameters on the hydrodynamic and thermal performance of microchannels with micropillar arrays and provides a trade-off analysis for the design and optimization of microchannel performance.

3.6 Limiting Case Single-Phase Heat Transfer Modeling

Heat transfer effects for single-phase laminar flow in the entrance and fully developed regions of a rectangular duct with different aspect ratios have been studied numerically [38]. The idea of breaking down complex geometries into smaller sections has been previously used to determine the analytical solution for the permeability of micropillar array based microchannels [26]. Developing an analytical solution for the heat transfer coefficient through this approach has its limitations. However, this approach provides a simplistic limiting case estimate for the single-phase heat transfer performance for such geometries.

As shown in Figure 3.17, a cell is divided into three sections A, B, and C. All these three sections have been modelled as rectangular ducts with the boundary conditions as shown in Figure 3.18. A no slip boundary condition is applied to the pillar walls, upper wall, and lower wall. A symmetry condition is used on the two side walls as they are symmetric throughout the wick. These boundary conditions are translated for the velocity profile in a rectangular duct and are shown in Figure 3.19.

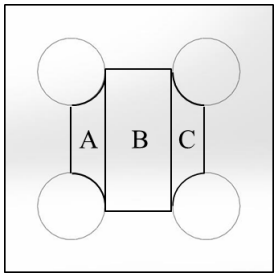

Figure 3.17: Schematic of the division of the wick into smaller sections

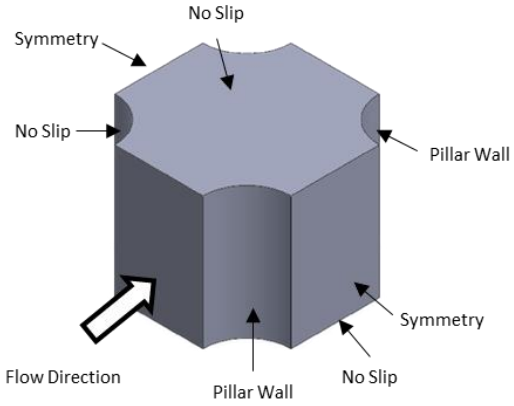

Figure 3.18: Boundary conditions for the rectangular duct flow assumption

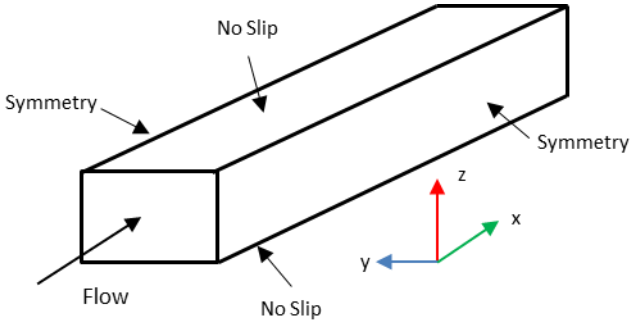

Figure 3.19: Rectangular duct schematic with the flow boundary conditions

The assumptions in this model are:

1. There is no slip at the upper and the lower wall. A symmetry boundary condition is employed for the two side walls to replicate the periodicity in the actual wick.
2. The flow is laminar and fully developed with no velocity and temperature gradients in the x-direction.
3. The velocity components in the y and the z-direction are negligible.
4. There is no energy generation or viscous energy dissipation.

The velocity profile for section B is given by:

$$u(x,y,z) = \left(1.5u_m cos\left(\frac{\pi}{s}y\right) + 1.5u_m\right)\left(1 - \left(\frac{2z}{h}\right)^2\right) \tag{24}$$

where u_m is the superficial velocity, s is half the channel width, and h is the channel height.

With the aforementioned assumptions, the energy equation for steady-state is given by:

$$\rho C_p u \frac{\partial T}{\partial x} = k\left(\frac{\partial^2 T}{\partial y^2} + \frac{\partial^2 T}{\partial z^2}\right) \tag{25}$$

where ρ is the fluid density, C_p is the fluid specific heat, u is the velocity profile, T is the temperature dependent on y and z, and k is the thermal conductivity of the fluid.

The heat transfer boundary conditions are:

- z = $-\frac{h}{2}$, uniform heat flux $q^{"}$
- z = $\frac{h}{2}$, adiabatic boundary condition
- y = $\pm$s, adiabatic boundary condition

To homogenize the boundary conditions, let:

$$\theta = T - \frac{q^{"}}{2kh}\left(z - \frac{h}{2}\right)^2 \tag{26}$$

Using mean temperature analysis:

$$\frac{\partial T}{\partial x} = \frac{\rho q^{"} p}{\dot{m} k} \tag{27}$$

where p is the total width of the channel, and $\dot{m}$ is the mass flow rate.

Substituting equation 26 and equation 27 into equation 25 we get:

$$\frac{\rho q^{"} p}{\dot{m} k} u - \frac{q^{"}}{kh} = \frac{\partial^2 \theta}{\partial y^2} + \frac{\partial^2 \theta}{\partial z^2} \tag{28}$$

The heat transfer boundary conditions for the homogeneous form of the above equation are given by:

- z = $-\frac{h}{2}, \frac{\partial\theta}{\partial z} = 0$
- z = $\frac{h}{2}, \frac{\partial\theta}{\partial z} = 0$
- y = $\pm$s, $\frac{\partial\theta}{\partial y} = 0$

To solve the above partial differential equation with homogeneous boundary conditions, the method of separation of variables is used. Using this method, we have:

$$\theta(y,z) = Y(y)Z(z) \tag{29}$$

Substituting the equation 29 in equation 28, the eigen function for this problem is given by:

$$Y(y) = cos\left(\frac{m\pi}{s}y\right), m = 0, 1, 2 \ldots \tag{30}$$

$$\theta(y,z) = Z_0(z) + \sum_{m=1}^{\infty} Z_m(z)\, cos\left(\frac{m\pi}{s}y\right) \tag{31}$$

Substituting equation 31 and equation 30 in equation 28 we get:

$$\frac{\rho q^{"} p}{\dot{m}k}u - \frac{q^{"}}{kh} = Z_0^{"}(z) + \sum_{m=1}^{\infty}\left[Z_m^{"}(z) - \left(\frac{m\pi}{s}\right)^2 Z_m(z)\right] cos\left(\frac{m\pi}{s}y\right) \tag{32}$$

Integrating the above equation over the interval [-s,+s] which spans the width of the channel, we get:

$$Z_0^{"}(z) = \frac{3q^{"}}{2kh}\left(1 - \left(\frac{2z}{h}\right)^2\right) - \frac{q^{"}}{kh} \tag{33}$$

$$Z_0(z) = \frac{3q^{"}}{2kh}\left(\frac{z^2}{2} - \frac{z^4}{3h^2}\right) - \frac{q^{"}z^2}{2kh} + c_1 z + c_2 \tag{34}$$

where c_1 and c_2 are constants.

Multiplying equation 32 by $cos\left(\frac{m\pi}{s}y\right)$ and integrating over the interval [-s,+s] we get:

$$for\ m = 1:\ Z_1^{"}(z) - \left(\frac{\pi}{s}\right)^2 Z_1(z) = \frac{3q^{"}}{2kh}\left(1 - \left(\frac{2z}{h}\right)^2\right) \tag{35}$$

$$for\ m \neq 1:\ Z_m^{"}(z) - \left(\frac{m\pi}{s}\right)^2 Z_m(z) = 0 \tag{36}$$

The particular and homogeneous solutions for the above equation are given by:

$$[Z_1(z)]_p = \alpha_1 e^{\frac{\pi z}{s}} + \beta_1 e^{-\frac{\pi z}{s}} \tag{37}$$

$$[Z_1(z)]_h = \frac{6q^{"}}{kh^3}\left(\frac{s}{\pi}\right)^2 z^2 + \frac{3q^{"}}{2kh}\left(\frac{s}{\pi}\right)^2\left(\frac{8}{h^2}\left(\frac{s}{\pi}\right)^2 - 1\right) \tag{38}$$

$$for\ m > 1: [Z_m(z)]_p = \alpha_m e^{\frac{m\pi z}{s}} + \beta_m e^{-\frac{m\pi z}{s}} \tag{39}$$

Substituting the equations 37, 38, and 39 in equation 31 we get:

$$T(x,y,z) = \frac{3q^{"}}{2kh}\left(\frac{z^2}{2} - \frac{z^4}{3h^2}\right) - \frac{q^{"}}{2k}\left(z - \frac{h}{4}\right) + c_1 z + c_2 + \sum_{m=1}^{\infty}\left(\alpha_m e^{\frac{m\pi z}{s}} + \beta_m e^{-\frac{m\pi z}{s}}\right)\cos\left(\frac{m\pi y}{s}\right) + \left(\frac{6q^{"}}{kh^3}\left(\frac{s}{\pi}\right)^2 z^2 + \frac{3q^{"}}{2kh}\left(\frac{s}{\pi}\right)^2\left(\frac{8}{h^2}\left(\frac{s}{\pi}\right)^2 - 1\right)\right)\cos\left(\frac{\pi y}{s}\right) + \frac{q"p}{\dot{m}C_p}x \quad (40)$$

Using the boundary conditions, we get:

$$T(x,y,z) = \frac{3q^{"}}{2kh}\left(\frac{z^2}{2} - \frac{z^4}{3h^2}\right) - \frac{q^{"}}{2k}\left(z - \frac{h}{4}\right) + \left(\frac{6q^{"}}{kh^3}\left(\frac{s}{\pi}\right)^2 z^2 + \frac{3q^{"}}{2kh}\left(\frac{s}{\pi}\right)^2\left(\frac{8}{h^2}\left(\frac{s}{\pi}\right)^2 - 1\right) - \frac{6q^{"}}{kh^2}\left(\frac{s}{\pi}\right)^3\left(\frac{e^{\frac{\pi z}{s}} + e^{-\frac{\pi z}{s}}}{e^{\frac{\pi h}{2s}} + e^{-\frac{\pi h}{2s}}}\right)\right)\cos\left(\frac{\pi y}{s}\right) + \frac{q"p}{\dot{m}C_p}x \quad (41)$$

The heat transfer coefficient, bulk fluid temperature and wall temperature are given by:

$$HTC = \frac{q"}{(T_{wall,mean} - T_{bulk,mean})} \quad (42)$$

$$T_{bulk,mean} = \frac{1}{Channel\ Area} \iint_{z=-\frac{h}{2},y=-s}^{z=\frac{h}{2},y=s} T(x,y,z)dydz \tag{43}$$

$$T_{wall,mean} = \frac{1}{Channel\ Width} \int_{y=-s}^{y=s} T(x,y,0)dy \tag{44}$$

Solving the above equations, we get:

$$HTC = \frac{20k}{7h} \qquad Nu = \frac{40}{7(1+r)} \tag{45}$$

HTC is the heat transfer coefficient, *k* is the fluid thermal conductivity, *h* is the height of the channel, *Nu* is the Nusselt number, and *r* is the aspect ratio for the rectangular duct.

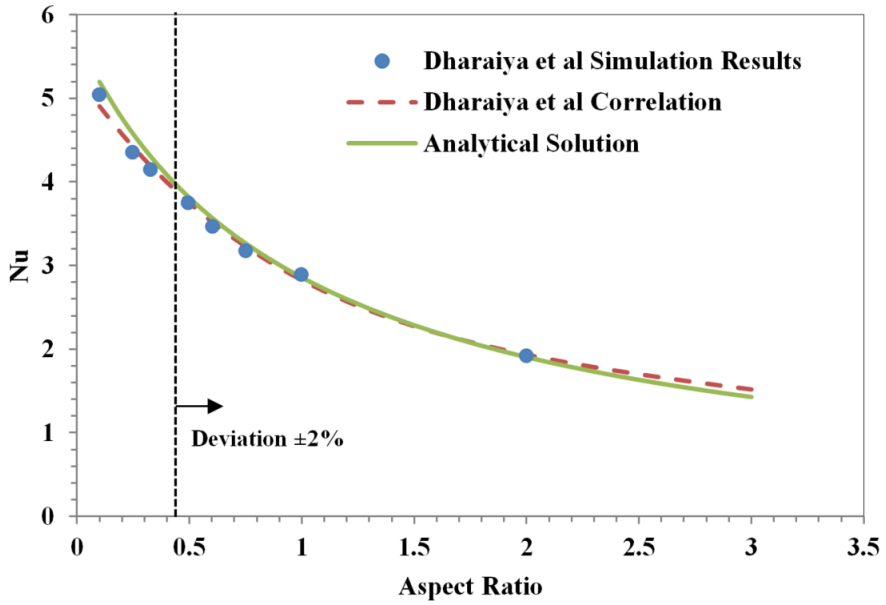

Figure 3.20: Comparison of the analytical solution with simulation results reported by Dharaiya et al

The results from the analytical solution are compared with the simulation and the corresponding correlation given by Dharaiya et al [38]. The Nusselt number from the analytical solution proposed in this section is within ±6% for the aspect ratio ranging from 0.1 to 3. The deviation drops down to ±2% for the aspect ratio ranging from 0.4 to 2.1.

This rectangular channel approximation from Figure 3.17 was used to estimate the heat transfer coefficient for micropillar array based microchannels. The analytical results were compared with simulations done in FLUENT for the unit cell with boundary conditions as shown in Figure 3.21. A no-slip condition was used for the upper wall, lower wall, and the pillar wall. A symmetry boundary condition was used on the side walls, and a periodic boundary condition was used for the inlet and the outlet of the unit cell. A uniform heat flux was given to the lower wall while all other walls were kept adiabatic. These simulations were performed for cylindrical pillars in a square shaped pillar arrangement with the spacing between the pillars varying from 25 µm to 125 µm for a pillar height of 75 µm.

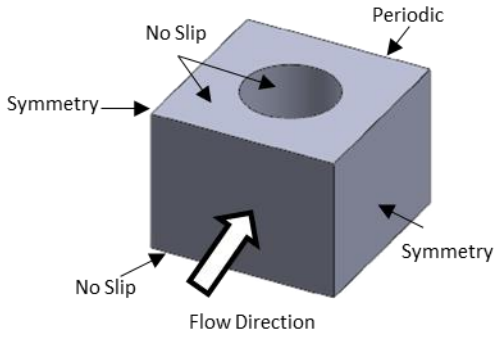

Figure 3.21: Computational domain for single-phase laminar convective heat transfer simulation

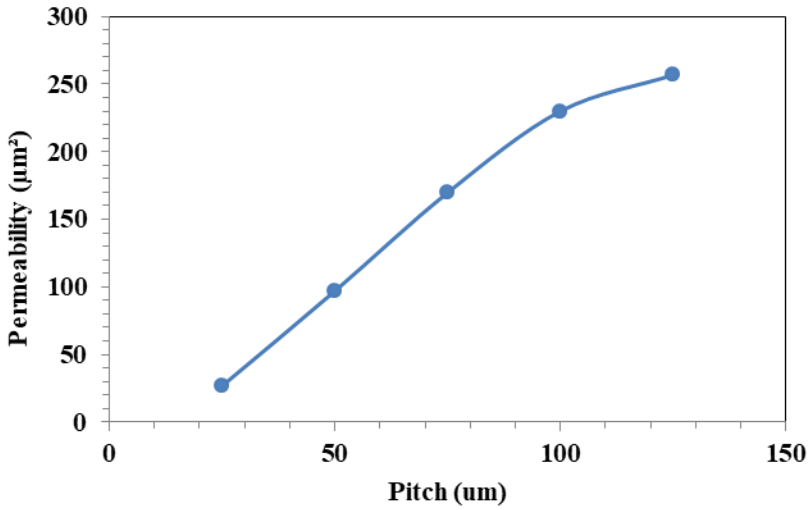

Figure 3.22: Permeability as a function of pillar spacing

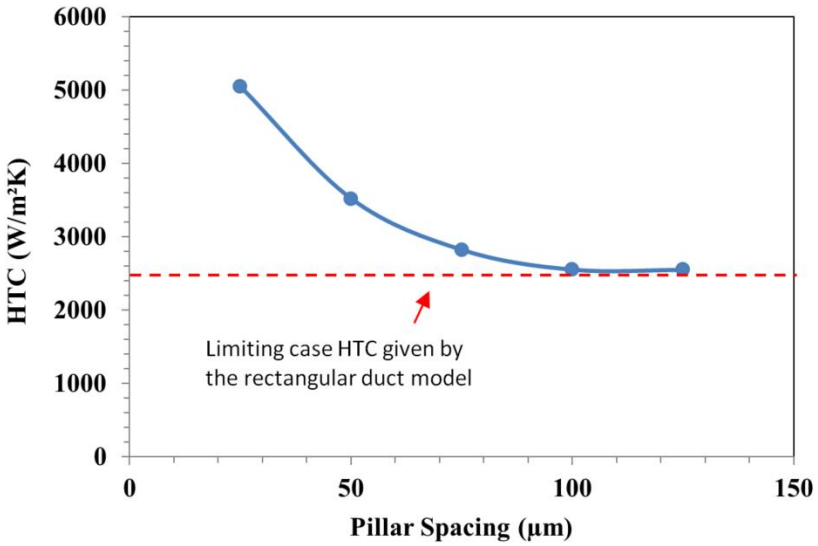

Figure 3.23: Heat transfer coefficient as a function of pillar spacing

The results from the simulations for the variation in permeability and the laminar flow single-phase heat transfer coefficient with respect to the pillar spacing are given in Figure 3.22 and Figure 3.23. As the pillar spacing increases, it provides more unobstructed space for the fluid to flow through resulting in a lower pressure drop and

higher permeability. For pillar spacing ranging from 25 µm to 100 µm, the permeability varies linearly with respect to the pillar spacing.

Comparing that with the single-phase laminar convective heat transfer coefficient for these geometries, lower the spacing between the pillars, higher is the heat transfer coefficient. This improvement in the single-phase laminar convective heat transfer performance comes at the expense of a higher pressure drop. This can be explained by the fact that as the porosity decreases, there is an increase in the mixing of the fluid which results in a better heat transfer performance. The effect of pillar spacing is more profound on the permeability as compared to the single-phase laminar heat transfer coefficient. As the spacing between the pillars increases, the HTC moves closer to the limiting case of a rectangular duct as shown in Figure 3.23. The analytical solution for a rectangular duct has its limitations in its application to a complex wick geometry given the assumptions made. This velocity component is of paramount importance as it is the primary cause of mixing within the fluid.

CHAPTER 4. CONCLUSIONS AND RECOMMENDATIONS

This research reports the single and two-phase flow characteristics and permeability measurements for flexible PDMS based microchannels with micropillar arrays. Three different micropillar arrangements with a porosity ranging from 0.8 to 0.91 have been tested. The experimental results have been coupled with numerical simulations and analytical modeling to address the deformability of low Young's Modulus PDMS microchannels and quantify it.

The addition of micropillars has its own advantages and disadvantages. While these micropillars aide the passive pumping of the fluid through capillary action, they also pose a significant pressure drop penalty for forced flow. For a given pillar geometry, denser the microchannel, better is the capillary pumping effect. However, with the need of augmented pumping for various applications, the corresponding pressure drop penalty is an important factor to be considered. The permeability of PDMS based microchannels has two unique characteristics. At lower flower rates, there is a significant contribution of the passive capillary pumping which improves the pressure drop characteristics of the microchannel. As the flow rate increases, an increase in the pressure within the microchannel results in a bulging effect which increases the cross-sectional area, and subsequently the porosity, for the fluid to flow through. This increases the permeability of the microchannel as compared to a conventional rigid microchannel. This is a welcome effect, as the hydrodynamic performance of the microchannel improves with an increase in the flow rate, reducing the pressure drop penalty. The relatively lower pressure within the microchannel at lower flow rates ensures that a lower porosity,

corresponding to better passive capillary pumping performance, is maintained. As the flow rates increase, the contribution of passive capillary pumping effect starts to fade away. Channels with a higher porosity are more susceptible to deformation given the relatively lower elastic resistance provided by the lesser number of micropillars. Thus, a channel with higher porosity deviates from a rigid-channel behavior more than a channel with lower porosity. This deformability of PDMS microchannels can be fine-tuned to specific requirements by changing the pillar geometry, pillar dimensions, PDMS mixing ratio, and PDMS curing temperature and time.

This research also reports on the single and two-phase flow characteristics of the dielectric fluid FC-3283 with a boiling point of 128°C. With the current advancements in flexible electronics and wearable technology, the unique thermal and electrical properties of PDMS provide significant opportunities in developing cooling solutions for such advanced electronics. A high thermal and electrical resistance, operating temperatures and durability make PDMS an ideal material for direct contact cooling applications. In this study, the single phase performance for three different pillar assemblies has been evaluated experimentally. Denser pillar geometry provides more stagnation zones and mixing which improves the overall heat transfer coefficient of the microchannel. High-Speed visualizations provide significant insights into the two-phase flow characteristics from onset of boiling, bubble nucleation, slug formation, and dry out. These results coupled with the hydrodynamic performance evaluate the overall wick performance.

The two analytical models developed that address the quantification of deformability and limiting case single-phase laminar heat transfer provide further analytical

information on the hydrodynamic and single-phase heat transfer performance of flexible PDMS microchannels.

The hydrodynamic, and single and two-phase convective heat transfer performance of deformable PDMS based microchannels have not been studied extensively. To better quantify the performance of such microchannels two studies can ideally be performed. On the hydrodynamic performance testing front, a correlation for the local expansion of a channel at a certain pressure, for a particular pillar assembly and a corresponding Young's Modulus will provide considerable parametric data for the design of flexible material based microchannels for various applications. On the thermal performance testing front, a study of the structural, fluid and thermal interactions will allow us to understand the behavior of these materials under single and two-phase flow conditions. Using local temperature and pressure sensors, a more detailed understanding of the complex fluid, structural and thermal interactions can be studied. This experimental data can be aided by computational simulations.

APPENDIX: UNCERTAINTY ANALYSIS

$$\text{Permeability: } K = \frac{\dot{m}\mu L}{\rho A \Delta P}$$

Measurement Uncertainties:

- Mass Flow Rate = ±1%
- ΔP (Pressure Drop) = ±2%
- Microfabrication Resolution = 3 μm
- Kinematic Viscosity = ±0.5%
- Density = ±0.65%

Experimental Uncertainty (w_E) = $\left[\sum_i \left(\frac{\partial E}{\partial x_i}\right)^2 w_{x_i}\right]^{1/2}$

where *w* is the uncertainty, *E* is the result and x_i are the independent variables

Substituting the measurement uncertainties into the experimental uncertainty equation we get,

$$w_K = \sim 5.5\%$$

$$q''_{eff} = q''_{total} - q''_{loss}$$

$$h_{overall,single-phase} = \frac{q''_{eff}}{\left(\bar{T}_{wall} - \frac{T_{in} + T_{out}}{2}\right)}$$

$$h_{overall,two-phase} = \frac{q''_{eff}}{(\bar{T}_{wall} - T_{sat})}$$

Measurement Uncertainties:

- Voltage = ±1%
- Current = ±1%
- Wall Temperature = ±0.2°C
- Fluid Temperature = ±1°C
- Saturation Temperature = ±1.9°C
- Microfabrication Resolution = 3 μm

Experimental Uncertainty (w_E) = $\left[\sum_i \left(\frac{\partial E}{\partial x_i}\right)^2 w_{x_i}\right]^{1/2}$

where *w* is the uncertainty, *E* is the result and x_i are the independent variables

Substituting the measurement uncertainties into the experimental uncertainty equation we get,

$$w_{q''_{eff}} = 2\%$$

$$w_{h_{overall,single-phase}} = 11.2\%$$

$$w_{h_{overall,two-phase}} = 9.8\%$$

REFERENCES

[1] S. G. Kandlikar, "History, Advances, and Challenges in Liquid Flow and Flow Boiling Heat Transfer in Microchannels: A Critical Review," *Journal of Heat Transfer,* vol. 134, no. 3, p. 034001, 2012.

[2] P. S. Lee, S. V. Garimella and L. Dong, "Investigation of heat transfer in rectangular microchannels," *International Journal of Heat and Mass Transfer,* vol. 48, no. 9, pp. 1688-1704, 2005.

[3] D. Lorenzini, C. Green, T. E. Sarvey, X. Zhang, Y. Hu, A. Fedorov, M. Bakir and Y. Joshi, "Embedded single phase microfluidic thermal management for non-uniform heating and hotspots using microgaps with variable pin fin clustering," *International Journal of Heat and Mass Transfer,* vol. 103, pp. 1359-1370, 2016.

[4] W. Li, X. Qu, T. Alam, F. Yang, W. Chang, J. Khan and C. Li, "Enhanced flow boiling in microchannels through integrating multiple micro-nozzles and reentry microcavities," *Applied Physics Letters,* vol. 110, no. 1, p. 014104, 2017.

[5] J. Lee and I. Mudawar, "Two-phase flow in high-heat-flux micro-channelheat sink for refrigeration cooling applications:Part I—pressure drop characteristics," *International Journal of Heat and Mass Transfer,* vol. 48, no. 5, pp. 928-940, 2005.

[6] J. Mathew, P. S. Lee, T. Wu and C. R. Yap, "Experimental study of flow boiling in

a hybrid microchannel-microgap heat sink," *International Journal of Heat and Mass Transfer,* vol. 135, pp. 1167-1191, 2019.

[7] Z. Wang, A. A. Volinsky and N. D. Gallant, "Crosslinking Effect on Polydimethylsiloxane Elastic Modulus Measured," *Journal of Applied Polymer Science,* vol. 131, no. 22, p. 41050, 2014.

[8] Materials Data Book, Cambridge, United Kingdom: Cambridge University Engineering Department, 2003.

[9] M. A. Hopcroft, W. D. Nix and T. W. Kenny, "What is the Young's Modulus of Silicon?," *Journal of Microelectromechanical Systems,* vol. 19, no. 2, pp. 229-238, April 2010.

[10] M. Liu, J. Sun and Q. Chen, "Influences of heating temperature on mechanical properties of polydimethylsiloxane," *Sensors and Actuators A: Physical,* vol. 151, no. 1, pp. 42-45, 2009.

[11] G. J. Jin, J. Uddin and J. S. Shim, "Biomimetic Cilia-Patterned Rubber Electrode Using Ultra Conductive Polydimethylsiloxane," *Advanced Functional Materials,* vol. 28, no. 50, p. 1804351, 2018.

[12] T. Gervais, J. El-Ali, A. Günther and K. F. Jensen, "Flow-induced deformation of shallow microfluidic channels," *Lab on a chip,* no. 4, pp. 500-507, 2006.

[13] P. Cheung, K. Toda-Peters and A. Q. Shen, "In situ pressure measurement within deformable rectangular polydimethylsiloxane microfluidic devices,"

Biomicrofluidics, vol. 6, no. 2, p. 026501, 2012.

[14] A. Raj and A. K. Sen, "Flow-induced deformation of compliant microchannels and its effect on pressure-flow characteristics," *Microfluid Nanofluid,* vol. 20, 2016.

[15] C. Kang, R. A. Overfelt and C. Roh, "Deformation properties between fluid and periodic circular obstacles in polydimethylsiloxane microchannels: Experimental and numerical investigations under various conditions," *Biomicrofluidics,* vol. 7, no. 5, p. 054102, 2013.

[16] C. Roh, J. Lee and C. Kang, "The Deformation of Polydimethylsiloxane (PDMS) Microfluidic Channels Filled with Embedded Circular Obstacles under Certain Circumstances," *Molecules,* vol. 21, 2016.

[17] C. Kang, C. Roh and R. A. Overfelt, "Pressure-driven deformation with soft polydimethylsiloxane (PDMS) by a regular syringe pump: challenge to the classical fluid dynamics by comparison of experimental and theoretical results," *Royal Society of Chemistry Advances,* vol. 4, pp. 3102-3112, 2014.

[18] W. Li and Y. Joshi, "Capillary-assisted evaporation/boiling in PDMS microchannel integrated with wicking microstructures," *Langmuir,* vol. 9, no. 2, pp. 12143-12149, 2020.

[19] S. Korniliou, C. Mackenzie-Dover, J. R. Christy, S. Harmand, A. J. Walton and K. Sefiane, "Two-dimensional heat transfer coefficients with simultaneous flow visualizations during two-phase flow boiling in a PDMS microchannel," *Applied*

Thermal Engineering, vol. 130, pp. 624-636, 2018.

[20] S. Bigham, A. Fazeli and S. Moghaddam, "Physics of microstructures enhancement of thin film evaporation heat transfer in microchannels flow boiling," *Scientific Reports*, vol. 7, p. 44745, 2017.

[21] S. Cho, R. Tummala and Y. Joshi, "Capillary Performance of Micropillar Arrays in Different Arrangements," *Nanoscale and Microscale Thermophysical Engineering*, vol. 22, no. 2, pp. 97-113, 2018.

[22] S. J. McClintock and F. A. Kline, "Describing uncertainties in single-sample experiments," *Mechanical Engineering*, vol. 75, no. 1, pp. 3-8, 1953.

[23] N. Kovalchuk and C. Hadjistassou, "Laws and principles governing fluid flow in porous media," *The European Physical Journal E,* vol. 42, no. 56, 2019.

[24] B. R. Gebart, "Permeability of Unidirectional Reinforcements for RTM," *Journal of Composite Materials*, pp. 1100-1133, 1992.

[25] J. E. Drummond and M. I. Tahir, "Laminar Viscous Flow Through Regular Arrays of Parallel Solid Cylinders," *International Journal of Multiphase Flow*, vol. 10, no. 5, pp. 515-540, 1984.

[26] A. Tamayol and M. Bahrami, "Analytical determination of viscous permeability of fibrous porous media," *International Journal of Heat and Mass Transfer*, vol. 52, no. 9-10, pp. 2407-2414, 2009.

[27] R. S. Hale, R. T. Bonnecaze and C. H. Hidrovo, "Optimization of capillary flow through square micropillar arrays," *International Journal of Multiphase Flow*, vol. 58, pp. 39-51, 2014.

[28] R. S. Hale, R. Ranjan and C. Hidrovo, "Capillary flow through rectangular micropillar arrays," *International Journal of Heat and Mass Transfer*, vol. 75, pp. 710-717, 2014.

[29] K. Yazdchi, S. Srivastava and S. Luding, "Microstructural effects on the permeability of periodic fibrous porous media," *International Journal of Multiphase Flow*, vol. 37, no. 8, pp. 956-966, 2011.

[30] R. Xiao, R. Enright and E. N. Wang, "Prediction and Optimization of Liquid Propagation in Micropillar Arrays," *Langmuir*, vol. 26, no. 19, pp. 15070-15075, 2010.

[31] N. Srivastava, C. Din, A. Judson, N. C. MacDonald and C. D. Meinhart, "A unified scaling model for flow through a lattice of microfabricated posts," *Lab on a Chip*, no. 10, pp. 1148-1152, 2009.

[32] J. Happel and H. Brenner, Low Reynolds Number Hydrodynamics, vol. 1, New York: Prentice Hall, 1965.

[33] T. Chen and S. V. Garimella, "Flow Boiling Heat Transfer to a Dielectric Coolant in a Microchannel Heat Sink," in *ASME InterPACK*, San Francisco, California, USA, 2005.

[34] T. Harirchian and S. V. Garimella, "Microchannel size effects on local flow boiling heat transfer to a dielectric fluid," *International Journal of Heat and Mass Transfer,* vol. 51, no. 15-16, pp. 3724-3735, 2008.

[35] F. Yang, M. Alwazzan, W. Li and C. Li, "Single- and Two-Phase Thermal Transport in Microchannels with Embedded Staggered Herringbone Mixers," *Journal of Microelectromechanical Systems,* vol. 23, no. 6, pp. 1346-1358, 2014.

[36] F. Zhou, W. Zhou, C. Zhang, Q. Qiu, D. Yuan and X. Chu, "Experimental and numerical studies on heat transfer enhancement ofmicrochannel heat exchanger embedded with different shape micropillars," *Applied Thermal Engineering,* vol. 175, p. 115296, 2020.

[37] R. Ranjan, A. Patel, S. V. Garimella and J. Y. Murthy, "Wicking and thermal characteristics of micropillar structures for use in passive heat spreaders," *International Journal of Heat and Mass Transfer,* vol. 55, no. 4, pp. 586-596, 2012.

[38] V. V. Dharaiya and S. G. Kandlikar, "Numerical Investigation of Heat Transfer in Rectangular Microchannels Under H2 Boundary Condition During Developing and Fully Developed Laminar Flow," *Journal of Heat Transfer,* vol. 134, no. 2, p. 020911, 2012.